Facies (2026) 72:7
https://doi.org/10.1007/s10347-025-00719-z

ORIGINAL ARTICLE

Fluctuating seafloor oxygenation before, during and after the Frasnian/Famennian crisis: Quantitative colour analysis and geochemistry of Upper Devonian marine red beds, Montagne Noire, S. France

Ondřej Bábek[1] · Tomáš Kumpan[2] · Stanislava Vodrážková[3] · Catherine Girard[4]

Received: 31 October 2025 / Accepted: 16 December 2025 / Published online: 13 January 2026

Abstract

Early diagenetic precipitation of red iron oxide (hematite) in most marine red beds (MRB) makes these sediments suitable archives for seafloor redox conditions. A composite succession of upper Frasnian to lower Famennian red pelagic limestones was studied at two sections in the Montagne Noire, South of France including the Coumiac base of the Famennian GSSP section containing the Upper and Lower Kellwasser (LKW and UKW) horizons of global dysoxia/anoxia. Data from facies analysis, gamma-ray spectrometry, magnetic susceptibility, Vis-diffuse reflectance and X-ray fluorescence spectroscopy with 5 to 25 cm resolution at the section were supplemented by optical and scanning electron microscopy, electron microprobe analysis and laser-ablation inductively coupled mass spectrometry of thin sections. Submicron hematite crystals in the red facies are closely associated with authigenic clays, pitted microspar, microstromatolites, microborings, and *Frutexites* microproblematica indicating a microbial control on its precipitation at or very close to the sediment–water interface. The hematite precipitation was driven by iron cycling accompanied by cycling of redox-sensitive elements (Mn, Cu, V, Mo, U) along (micro-)redox gradients within the sediments under oxic seafloor conditions, supported by low sedimentation rates. The red stratigraphic succession is punctuated by eight, ~ 0.5 to ~ 1.5 m thick horizons including the LKW and UKW, with non-red colours and elevated concentrations of redox-sensitive elements reflecting various stages of bottom dysoxia to anoxia. The horizons show a recurrence time of ~ 0.85 Myr to ~ 2.0 Myr and they are interpreted as repeated phases of seafloor dysoxia/anoxia due to vertical fluctuations of the oxygen minimum zone culminating during the Frasnian/Famennian crisis.

Keywords Marine red beds · Diffuse reflectance spectroscopy · Geochemistry · Seafloor redox · Palaeoceanography · Rheic ocean · FrasnianFamennian crisis

Introduction

Marine red beds (MRB) are mostly deep marine sediments with a distinct red colour caused by the presence of hematite and, to a lesser extent, goethite and Mn^{2+}-bearing calcite (Jenkyns and Hsü 1975; Franke and Paul 1980; Wang et al. 2005; Hu et al. 2012). The MRBs are typically pelagic, nodular limestones and marls with predominance of nektonic, planktic and benthic skeletal heterotrophs, deposited at very low sediment accumulation rates (typically from a few mm/kyr to ~ several 10s mm/kyr) in deep ramp to open ocean environments, commonly of Ordovician, Silurian, Devonian, Jurassic and Cretaceous age (Jenkyns 1975; Franke and Paul 1980; Préat et al. 1999; Mamet and Préat 2006;

✉ Ondřej Bábek
ondrej.babek@upol.cz

1 Department of Geology, Palacký University, 17. Listopadu 12, Olomouc 77146, Czech Republic

2 Department of Geological Sciences, Masaryk University, Kotlářská 2, 61137 Brno, Czech Republic

3 Czech Geological Survey, Geologická 6, 152 00 Prague, Czech Republic

4 UMR 5554, Institut Des Sciences de L'Evolution C.C. 64, Université Montpellier 2, CNRS, Place Eugène Bataillon, 34095 Montpellier, France

Wagreich and Krenmayr 2005; Wang et al. 2005; Gawlick et al. 2006; Neuhuber et al. 2007; Jansa and Hu 2009; Ferretti et al. 2012; Hu et al. 2012; Devleeschouwer et al. 2015; Bábek et al. 2018, 2021).

The presence of hematite in MRBs is important because, being a ferric oxide, it may indicate oxic conditions in marine, seafloor environments. Although the hematite may rarely be sourced from the red terrigenous deposits (Giosan et al. 2002; Rong et al. 2012) widespread petrological and geochemical evidence suggests that the hematite is authigenic and early diagenetic in origin in most MRBs (Franke and Paul 1980; Mamet and Préat 1997; Cai et al. 2012). The low sediment accumulation rates coupled with oligotrophic conditions in water column and oxygen contents in bottom waters may have favoured prolonged oxidation of sediment close to the sediment–water interface (Tremolada et al. 2006; Hu et al. 2012; Bábek et al. 2018), similar to red pelagic clays on the present-day ocean floors (Gleason et al. 2002). The hematite growth might have been mediated by the activity of Fe(II)-oxidizing bacteria in near-bottom environments with limited oxygen supply (Mamet and Préat 2006; Préat et al. 2011). Oxidation of organic matter by microbial respiration is generally assumed to result in progressive consumption of O_2, nitrate, manganese, iron, and other electron acceptors along a redox gradient below the seafloor (Strumm and Morgan 1996; Algeo and Li 2020; Munnecke et al. 2023). These redox reactions take place in oxic, dysoxic, suboxic and anoxic/euxinic aqueous conditions, which reflect the level of dissolved O_2 and H_2S, and which are imprinted in the sediment through different concentrations of redox-sensitive elements (for a comprehensive review see Algeo and Li 2020). Consequently, suitable conditions for hematite growth gradually dissipate below the seafloor, leading to a colour stratification due to an interplay between bottom oxygenation and sediment accumulation rates (Bábek et al. 2021). The distributions of Fe(II), Fe(III) and other redox-sensitive elements, including Mn, U, Mo, V, As, Cu and REE, coupled with the hematite petrology, are powerful tools to interpret ancient redox conditions of the MRB, which may have comparable palaeoenvironmental significance to black shales in terms of palaeoredox conditions and ocean ventilation (Jansa and Hu 2009; Hu et al. 2012; Bábek et al. 2021).

The Frasnian/Famennian (F/F) crisis was a period of global environmental perturbations that were accompanied with major biodiversity loss (one of the big five mass extinctions) affecting marine and terrestrial biota including corals, stromatoporoids, trilobites, cephalopods, tentaculitids, conodonts and miospores (Sepkoski 1982; Cooper 1986; Schindler 1993; Becker and House 1994; Streel et al. 2000; House 2002; Bond et al. 2008; Racki et al. 2018; Qie et al. 2019). The F/F is accompanied by two distinct layers in deep-shelf carbonate sediments, the Lower and Upper Kellwasser Horizons (LKW, UKW), with positive stable carbon isotope excursions in carbonate and organic carbon indicating enhanced global rates of burial of organic carbon (Joachimski and Buggish 1993; Wang et al. 1996; Joachimski 1997; Chen et al. 2002). The LKW and UKW horizons are also accompanied by positive excursions in total organic carbon contents, elemental proxies of bottom dysoxia and enhanced organic productivity (U, Mo, V, Cu, Ni, P, Si), Hg as a proxy of volcanic influence, uranium isotopes, biomarkers and negative magnetic susceptibility excursions at several sections (Wang et al. 1996; Racki et al. 2002, 2018; Pujol et al. 2006; Riquier et al. 2007; Marynowski et al. 2012; Song et al. 2017). At other sections, however, such sedimentological, geochemical and petrophysical patterns may be missing or may differ (George et al. 2014; Weiner et al. 2017). The F/F crisis was likely caused by vigorous global climate fluctuations on the background of overall Late Devonian climatic cooling, associated with carbon cycle perturbations, high-frequency fluctuations of marine anoxia, sea level and terrigenous supply from the continents, modulated by orbital cycles, which might have been ultimately caused by enhanced volcanic activity (Joachimski and Buggish 1993; Ellwood et al. 2000; Chen and Tucker 2003; De Vleeschouwer et al. 2013; Racki et al. 2018; Da Silva et al. 2020; Song et al. 2017; Algeo et al. 2025). However, an alternative explanation for the mass extinction has been offered linking the Late Devonian spread of vascular land plants, as the primary bioevolutionary trigger, to subsequent accelerated weathering rates, nutrient fluxes to oceans, algal blooms and massive water column deoxygentation (Algeo et al. 1995; Algeo and Shen 2024).

The basal Famennian Global Stratotype Section and Point (GSSP) at Coumiac, Montagne Noire, France exposes an about 30 m thick succession of red and grey, deep-water and pelagic argillaceous and micritic carbonates (Becker et al. 1989; Klapper et al. 1993; Préat et al. 1998, 1999) including the LKW, UKW horizons and the markedly red nodular (ferruginous) ammonoid carbonates of the Famennian “Griotte” facies. The red- and grey- coloured sediments alternate in several distinct layers across the F/F boundary, with the LKW and UKW representing the most distinct non-red layers. Considering hematite as an indicator of bottom redox conditions in marine settings, the MRBs of the “Griotte” facies and non-red carbonates of the LKW and UKW horizons at Coumiac may represent end-members of the bottom redox conditions during the end Frasnian – Famennian interval. The aim of this study is to explore the petrological, geochemical and colour record of palaeoredox conditions before, during and after the critical F/F interval of global marine anoxia in the Montagne Noire, France, using the MRBs as appropriate palaeoenvironmental archives. Two well-dated sections, Coumiac (Frasnian/Famennian, Préat et al. 1998) and Col des Tribes (Famennian, Girard et al. 2014) are investigated with the focus on outcrop gamma-ray spectrometry, high resolution sampling (up to 5 cm across the critical horizons), element geochemistry and quantitative colour representation using diffuse reflectance spectroscopy.

Geological settings and stratigraphy

The studied sections, Coumiac and Col des Tribes, are situated in abandoned quarries in the Montagne Noire, near the village of Causses-et-Veyran, about 19 km NW of Béziers, and about 65 km WSW of Montpellier, southern France (Fig. 1). The sections are located about 2.5 km apart. The Montagne Noire forms part of the Variscan Massif Central represented by metamorphic domes composed of Proterozoic to Lower Palaeozoic gneisses and schists, and its cover comprising unmetamorphosed Palaeozoic sediments (Aerden 1998). Its present-day structure was formed by multiphase Variscan crustal thickening during the late Devonian to Westphalian (Moscovian) period, followed by Westphalian gravitational collapse causing sub-horizontal low-angle thrusting (Aerden 1998). The studied sections are located in the southern part of the Montagne Noire called the “Nappes du Versant Sud” representing a pile of km-scale recumbent fold nappes composed of Palaeozoic sediments, and acid and intermediate volcanic rocks (Arthaud 1970; Franke et al. 2010b, a). The structurally highest unit of the nappe pile is the Mont-Peyroux nappe, in which the Coumiac and Col des Tribes successions are exposed.

The Mont-Peyroux nappe sequence comprises a Lower Devonian (“Gedinnian”, Lochkovian) to Lower Carboniferous (Viséan to Serpukhovian) succession that rests unconformably upon Ordovician siliciclastic sediments (Feist 1985). The succession consists of dolomites, bioclastic limestones, nodular limestones, radiolarian cherts, carbonate turbidites and debris flow units and siliciclastic turbidites (synorogenic flysch) formally assigned to several formations, showing a deepening-upward trend (Feist 1985; Franke et al. 2010b, a). The Coumiac section exposes a succession of carbonates, shales and cherts of the Lower, Middle and Upper Coumiac Formation (lower Frasnian to Famennian, *Pa. minuta* Zone) overlain by nodular limestones and shales of the Griotte Formation (Famennian, upper *Pa. minuta* to middle Famennian) (Feist et al. 1985; House et al. 1985; Klapper et al. 1993). The Col des Tribes section exposes a succession of the Coumiac, Griotte and Saint Nazaire Formations of uppermost Frasnian (FZ13) to lower Tournaisian (*Si. quadruplicata* Zone) age (Feist et al. 1985; Girard et al. 2014; Feist et al. 2021). In view of poor exposure of most of the section, only the well-exposed part between samples #35 (Famennian, *Pa crepida* Zone) and #48 (*Pa. marginifera* Zone) of Girard et al. (2014) were included in this study. Sedimentology and microfacies of the sections have been described by Préat et al. (1998) at

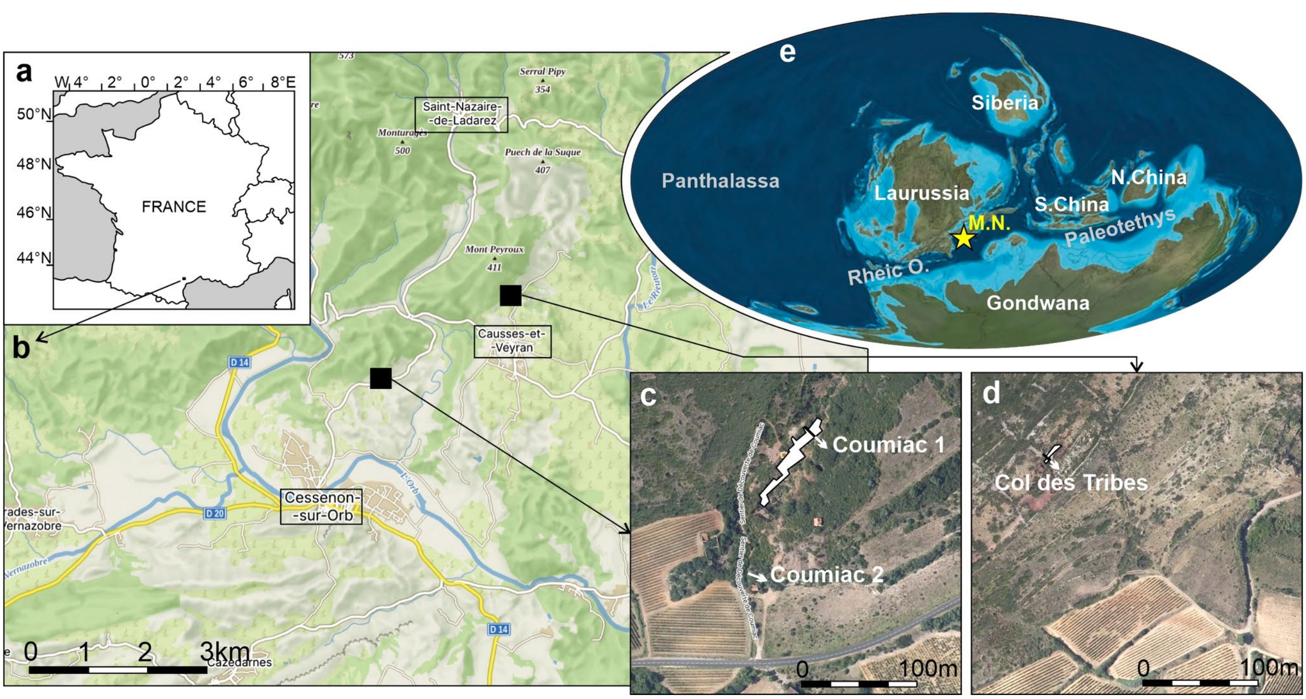

Fig. 1 (**a – d**): geographic location of the measured sections, Coumiac and Col des Tribes in old quarries near the village of Causses-et-Veyran, Montagne Noire, southern France (mapy.com); (**e**) palaeogeographic map of the Late Devonian (~370 Ma) world, adopted from Blakey and Ranney (2018)

Coumiac and by Girard et al. (2014) at Col des Tribes. Geochemistry and magnetic susceptibility of the Coumiac section was reported by Le Houdec (2013) and Girard et al. (2014).

Conodont alteration index (CAI) values in the limestones in the studied area of the Mont-Peyroux Nappes (Roquebrun Synform) range from 2.0 to 3.0 and increase to 4.5 to the north (Wiederer et al. 2002). This is supported by illite crystallinity (IC) measurements from the surrounding siliciclastics of the Culm facies, ranging from 0.23 to ~ 0.8 and decreasing northward. This thermal maturity pattern indicates that the Roquebrun Synform experienced dynamic contact metamorphic temperatures reaching approximately 225 °C in the northern areas (anchimetamorphic conditions), decreasing southward to diagenetic conditions, with temperatures around 80 °C, reflecting increasing distance from the metamorphic heat source (Wiederer et al. 2002). The CAI values at the Coumiac 1 section range from 2.5 to 3.0 (Girard et al. 2014), and 1.5 to 2 at the Coumiac 2 section (reported herein).

Material and methods

Two sections were studied, Coumiac (GPS: 43°28′9.987"N, 3°3′31.095"E) and Col des Tribes (GPS: 43°28′54.599"N, 3°5′5.994"E) with total thicknesses of 42.5 and 23 m, respectively. The Coumiac is a composite section consisting of the lower part (Coumiac 1, the main section described by Klapper et al. 1993) and an upper part (Coumiac 2) located about 100 m S of the main section (Fig. 1). The sections were cleaned, described bed-by-bed with focus on bed thickness and geometry, lithology, grain size and sedimentary structures. Conodont biostratigraphy data for the Coumiac 1 and Col des Tribe were adopted from Klapper (1989), Klapper et al. (1993) and Girard et al. (2014). Additionally, five conodont samples were collected from the Coumiac 2 section. The samples were dissolved by maceration in 15% acetic acid and conodont hand-picked from insoluble residues. The Frasnian conodont zones (FZ) (Klapper 1989) and revised standard Famennian conodont zonation of Spalletta et al. (2017) are used as the biostratigraphic framework in this study.

The sections were logged by outcrop gamma-ray spectrometry with a regular thickness step of 25 cm (total 212 measurements) using a GT-32 spectrometer (Georadis, Czechia) with a BGO (Bismuth Germanate Oxide) and assay time of 180 s. The instrument calculates K (%), U (ppm) and Th (ppm) concentrations based on characteristic gamma-ray spectral lines from element decays emitted from the rock surface. The instrument was calibrated by the manufacturer using large concrete pads with known K, U and Th contents. The K and Th concentrations were used to convert the signal to computed (clay) gamma ray (CGR, API units) as a proxy of clay content in carbonate rocks, using the Schlumberger formula (Rider 1999; Bábek et al. 2013).

The sections were sampled with a regular thickness interval of 10 cm (Col des Tribes) and 20 cm (Coumiac) with more detailed (5 cm interval) sampling across the LKW and UKW units (318 samples in total). Bulk magnetic susceptibility (MS) was measured on cleaned and dried samples using a KLY-2 kappabridge (Agico, Czechia) at a magnetic field intensity of 300 $A.m^{-1}$, operating frequency of 920 Hz and sensitivity of 4.10–8 SI. The samples were weighed and the bulk MS converted to mass-specific MS expressed in $m^3.kg^{-1}$. The error of measurement due to room conditions stabilizing, shape parameters and orientation of the sample during the repeated measurements did not exceed ± 2%.

The samples (n = 318) were then powdered to analytical fineness (< 63 m), sealed in transparent polyethylene foil bags and measured for diffuse reflectance spectroscopy (DRS) by a handheld SP62 (X-Rite Inc., U.S.A.) visible light (Vis) sphere spectrophotometer with an 8 mm aperture, gas-filled tungsten lamp light source and d/8 measurement geometry. The instrument was calibrated against a black-and-white (white ceramic plate) standard provided by the manufacturer. The reflectance of the foil was subtracted from the sample reflectance. The measurements were processed by X-Rite Color Master software, and the output data were represented in a Vis wavelength band (400 to 700 nm) reflectance curve with readings taken in 10 nm increments and the Commission Internationale de lÉclairage CIE*L*a*b** colour data taken in the D65/10º Illuminant/Observer mode. The red band reflectance was calculated as the proportion of sum reflectance in the red wavelength band (625–700 nm) to the total reflectance in the Vis light spectrum (Zhang et al. 2007). Relative proportions of goethite and hematite were inferred from the first derivatives of the reflectance curve using the approach of Deaton and Balsam (1991). Techniques to determine absolute contents of hematite and goethite using DRS, e.g., by adding known amounts of the pigments to deferrated samples (Zhang et al. 2007), were not used in this study.

The concentrations of 18 elements (Al, Si, P, K, Ca, Ti, V, Mn, Fe, Ni, Cu, Zn, As, Rb, Sr, Zr, Mo and Pb) were analysed on a subset of the powdered samples (n = 299) by energy-dispersive X-ray fluorescence (EDXRF) using a Delta Premium EDXRF spectrometer (Innov-X, USA) with silicon-drift detector, 2 × 120 s acquisition time, and 15 and 40 kV accelerating voltage. The samples were measured in plastic containers sealed by Mylar foil. The EDXRF results given in ppm were calibrated by high-precision inductively-coupled-plasma mass spectrometry (ICP-MS). An in-house set of 76 samples from Lower Devonian red marine carbonates and shales of the Prague Basin (Palacky University, Olomouc) were measured by EDXRF using the same XRF device and analytical conditions, and by ICP-MS after total acid digestion (Table S1, Supplementary material). Linear regression equations of the ICP-MS vs. EDXRF data in bivariate plots were used to convert the EDXRF concentrations to ICP-MS values (analytical accuracy). Correlation coefficients from the regression were used as a measure of the EDXRF analytical precision. The correlation coefficients (R^2) were very high (>0.99) for Al, Si, Fe, Ca, Mn, K, Rb, Zn, Ti and Zr, slightly lower (>0.95) for As, Sr and Pb, lower (>0.90) for Ni and V, and even lower (>0.87) for Cu and Mo. Phosphorus was not calibrated due to its low R^2 value.

A set of 43 bulk-rock samples from the Coumiac section were analysed for their trace element contents (Be, Cr, Co, Ni, Cu, Zn, As, Rb, Sr, Y, Zr, Nb, Mo, Cs, Ba, La, Ce, Pr, Nd, Sm, Eu, Gd, Tb, Dy, Ho, Er, Tm, Yb, Lu, Hf, Pb, Th and U) using an ICP-MS Thermo ICAP Q (Thermo Fisher Scientific, Waltham, MA, USA) in the Laboratories of the Geological Institutions, Charles University, Prague. Prior to the analysis, the samples were totally digested in a mixture of concentrated HF–$HClO_4$ at 150 °C followed by several treatments in concentrated HNO_3. The analytical accuracy of the ICP-MS methods within 10% against the certified or recommended values was regularly monitored using SBC-1 reference materials (USGS).

Eight covered and 17 polished thin sections from Col des Tribes, and 16 covered and 41 polished thin sections from Coumiac were prepared, and studied under optical microscopy using Zeiss Axio Imager A2m microscope. Detailed mineralogy and petrology of carriers of the red colouration in the thin sections were studied under a field emission gun – scanning electron microscope (FEG-SEM) using Tescan Mira 3GMU (Tescan Orsay Holding a.s., Czechia) with backscattered electron (BSE) and secondary electron (SE) detectors. The SEM is equipped with two energy-dispersive X-ray fluorescence EDS SDD X-Max 80mm^2 analyser (Oxford Instruments, Abingdon, UK) with an active area of 100 mm^2, operating at 15 kV accelerating voltage, 1.5 nA beam current and 15 mm working distance. For the SEM analysis, the thin sections were acid-etched using 5% CH_3COOH (acetic acid) for 10 s, and coated with a 15 nm amorphous carbon layer to prevent charging.

A total of 184 point-analyses from 11 thin sections were analysed by inductively coupled plasma mass spectrometry with laser ablation (LA-ICP-MS) using a high-resolution sector-field Element 2 spectrometer (Thermo Fisher Scientific, Waltham, MA,USA) fitted with Analyte G2 (Photo Machines Inc., Redmond, WA, USA) excimer laser. Details of the analytical conditions, list of isotopes and calibrations are described in Kalvoda et al. (2018). The output raw data were given in counts per second, and converted to concentration units (ppm) using the sum of element oxides (and Ca as $CaCO_3$) as 100% concentration verified by electron microprobe analysis in wavelength dispersive X-ray fluorescence mode (cf., Bábek et al. 2021). Enrichment factors of trace elements and rare-earth element (REE) concentrations were normalized using the Average Upper Continental Crust (UCC) standard (McLennan 2001).

Results

Lithology, facies and facies stacking patterns

Beds at both sections are nearly perfectly vertical due to folding and are lithologically relatively uniform. Two major facies and several subfacies have been identified (Fig. 2). In the field, facies F1 appears as nodular, marly or argillaceous, fine-grained carbonate (lime mudstone/wackestone) of variable colour from grey, yellowish, pink to red, with bioclasts of crinoids, sparse goniatites, bivalves and orthoconic nautiloids visible by naked eye, and other, unidentifiable bioclasts. In places, the crinoid fragments form several cm-thick, lens-like accumulations indicating hydrodynamic reworking (Fig. 2f). Sparsely, the sediment is bioturbated. The calcareous nodules are usually small, from a few to 20–30 mm in diameter, embedded in more marly, commonly darker or a deep red matrix, in places impregnated by black Mn-oxides (Fig. 2a). The sediment contains abundant irregular bands, several cm thick, of a deeper red colour with red coatings around bioclasts, as well as hardgrounds, calcite veins and stylolites (Fig. 2b). Beds of the facies F1 are 3 cm to 20 cm thick, separated by thin shaly and marly laminae (Col des Tribes, 0 to ~7.5 m). The subfacies F1a is a homogeneous or weakly nodular wackestone with goniatites, crinoids and orthoconic nautiloids, arranged into thin, sheet-like beds with a grey to pink colour (Fig. 2b). The beds can be slightly bioturbated and contain stromatactis structures with digitated roof, especially between the LKW and UKW horizons (Fig. 2e). Near the LKW horizon in Coumiac (14.8 m), this facies also contains distinct, about 3 cm thick, bed-parallel stromatolitic coatings. The subfacies F1b ("Griotte" limestone) is a strongly argillaceous nodular limestone containing abundant goniatites, in places with geopetal fillings, common Mn-oxides coatings on bioclasts, on bedding planes and in the matrix between nodules (Col des Tribes, ~7.5 to ~10 m, Fig. 2a). The subfacies F1c is a megabreccia (Col des Tribes, ~10 to ~12 m) comprising contorted layers and large (>1.5 m long) clasts of the nodular F1 facies with a chaotic arrangement demonstrating soft-sediment, likely gravitational deformation (Fig. 2d). The facies F2 is dark grey, or greenish marly shale, in places

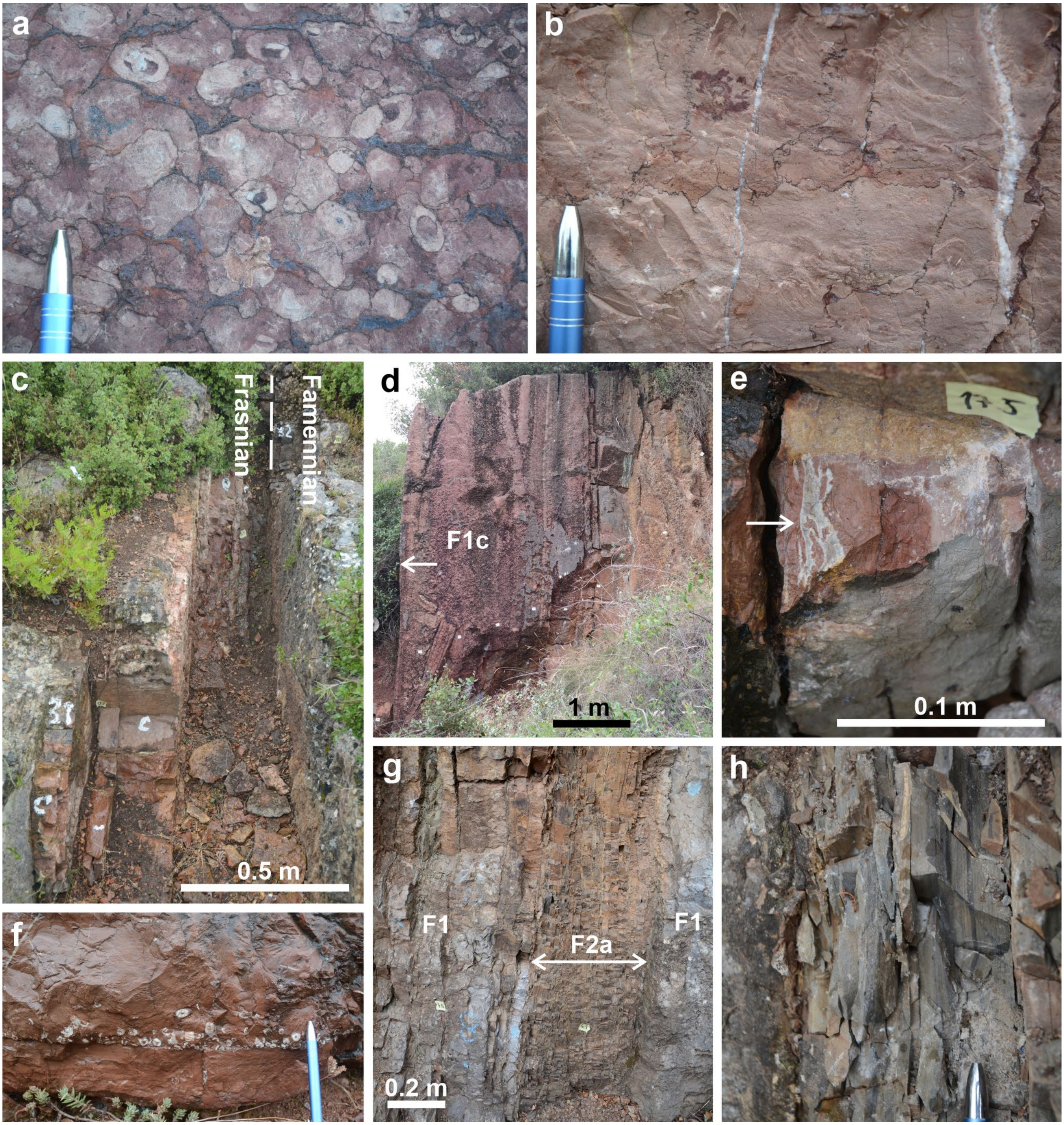

Fig. 2 Field appearance of the studied rocks; (**a**) subfacies F1b, "Griotte" limestone, nodular wackestone with goniatites and Mn-oxide impregnations in the matrix between nodules, Famennian, Col des Tribes; (**b**) facies F1, red nodular, skeletal wackestone with irregular darker-red bands (some hardgrounds) and stylolites, Famennian, Col des Tribes; (**c**) Upper Kellwasser (UKW) horizon showing nodular carbonates, facies F1, with increasing argillaceous contents towards the Frasnian/Famennian boundary (arrow), Coumiac; (**d**) megabreccia, subfacies F1c, with large contorted clasts of red nodular limestone, Famennian, Col des Tribes (arrow shows stratigraphic way up); (**e**) stromatactis (arrow) in red nodular limestone of subfacies F1a, Frasnian, Coumiac; (**f**) lens-like skeletal accumulation of crinoids in red nodular limestone, subfacies F1a, Famennian, Coumiac; (**g**) layer of cherty shale, facies F2 (arrow), sandwiched between grey nodular limestones, facies F1, Frasnian, Coumiac; (**h**) finely laminated succession of siltstone, fine-grained sandstone, shale and chert, F2 facies, Frasnian, Coumiac

alternating with thin beds of chert with radiolarians, and/or thinly laminated with silty or very fine-grained sandy laminae (Fig. 2c,h). Individual beds are from 0.12 to 0.7 m thick (Coumiac, 2.1 to 2.8 m; 4.3 to 4.7 m; 5.6 to 5.7 m). The subfacies F2a comprises several cm-thick layers of dark grey pure chert, in places laminated with thin shale laminae (Fig. 2g).

The bed stacking patterns at the sections are relatively simple. The lower part of the Frasnian succession in Coumiac is characterized by an alternation of F1 and F2 facies and their subfacies. The F2 facies gradually disappear upwards towards the end of the Frasnian; the last shaly layer is the LKW horizon. The uppermost Frasnian and lowermost Famennian succession is dominated by relatively pure carbonates (subfacies F1a) except for the UKW horizon (Coumiac). Higher up in the Famennian, the strongly nodular F1b subfacies ("Griotte" limestone) and the megabreccia (F1c) predominate, ultimately giving way again to relatively pure carbonates of subfacies F1a (Coumiac and Col des Tribes).

Microfacies and microscopic patterns of red colouration.

Detailed petrographic and microfacies analyses of both sections have been provided by Tucker (1975), Devleeschouwer (1999), Préat et al. (1999) and Girard et al. (2014). Here, we summarize the features that are most relevant to this study.

The lowermost part of the Coumiac section (facies F1) comprises grey, bioturbated skeletal wackestones with a microsparitic matrix, dominated by styliolinids and very rare benthic shell fragments, including trilobites, crinoids and ostracods, accompanied by unidentifiable shell hash (Fig. 3). Calcified radiolarians and hexactinellid sponge spicules were observed in places. The styliolinids show a chaotic arrangement without shell telescoping. These carbonates are intercalated with the thin-bedded shales (facies F2) exhibiting lamination ranging from planar-parallel to wavy-crinkled structures, in which the styliolinids occur either scattered throughout the matrix or concentrated in discrete layers, exhibiting a preferred orientation. Benthic bioclasts are absent in the shales. EDX analysis of the carbon-rich shales revealed framboidal pyrites up to 10 µm in diameter. The grey styliolinid wackestones in the lower part of the section contain small anhedral grains of arsenopyrite and pyrite bearing trace elements including Ni, Cu, Co, Pb and As.

Orange and reddish varieties of the F1 facies first appeared at 7.7 m, transitioning to true red limestones at 8.6 m at Coumiac. This colour change within the facies F1 coincides with an increase in bioclast abundance and taxonomic diversity of the fossiliferous wackestones, although benthic elements remain scarce and fragmentary, typically yielding only 1–5 specimens per thin section of trilobites, brachiopods, crinoids and sponge spicules. Ostracods are the most common benthic fauna. The fauna includes pelagic bivalve fragments, goniatites, orthoconic nautiloids, pelagic entomozoacean ostracods and rare calcified radiolarians. The matrix contains abundant unidentifiable shell hash (Fig. 3a-d). At certain levels, authigenic fluorapatite was observed scattered in the matrix, along with phosphatized bioclasts, confirmed through SEM–EDX analysis.

The Lower Kellwasser horizon at the levels 15.1–15.7 m is represented by dark-coloured, organic-rich wackestones containing micropeloids and clotted aggregates about 25 to 250 mm in size with diffuse boundaries and rich in organic matter, rare foraminifers (*Irregularina*), dacryoconarids, ostracods and bivalves. The second dark limestone horizon at 18.55 m corresponds to the Upper Kellwasser Event, characterized by wackestone with abundant organic matter, dacryoconarid tentaculites and common framboidal pyrite

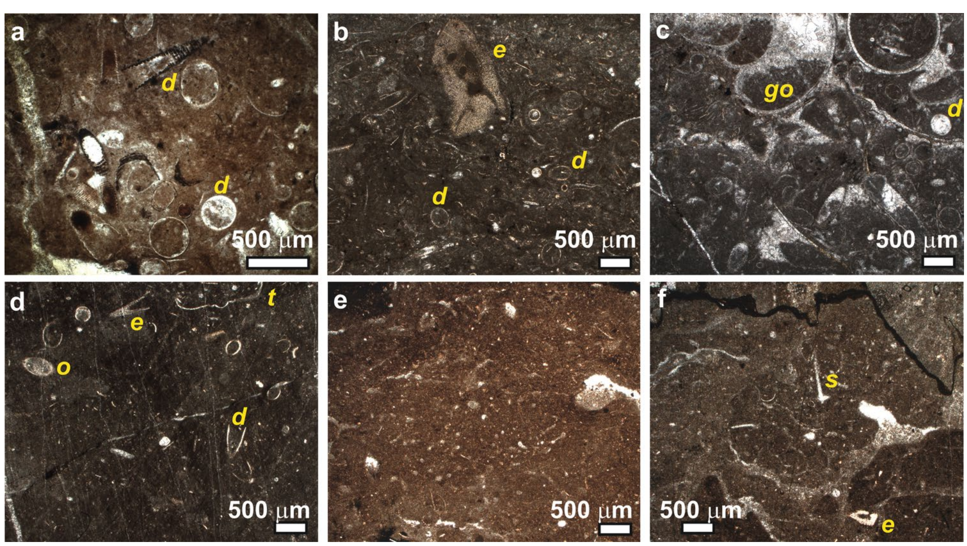

Fig. 3 (**a–d**): Examples of bioturbated, skeletal wackestones from the Coumiac and Col des Tribes sections, showing characteristic pelagic and benthic faunas; (**e–f**): fenestral structures with micropeloids and calcite-filled microproblematica within the matrix. Abbreviations used (yellow letters): s—sponge spicules, o—benthic ostracods, g—gastropods, d—dacryoconarids (locally with Fe-oxide coatings), go—goniatites, e—crinoids (with microboring in b), b—brachiopods. All images in plane-polarized light. Representative samples: a: CC 13.7, b: CC 16.45, c: CC 17.4, d: CC 8.6, e: CO 7.7, f: CO 8.5

(approximately 5 µm in size), as observed through SEM–EDX analysis. The yellowish beds overlying the Kellwasser horizons contain disseminated pyrite and an impoverished fauna, consisting mainly of pelagic bivalve fragments, small irregular fenestral structures and calcified radiolarians.

The Famennian parts of both sections (facies F1 and its subfacies) are characterized by fossiliferous wackestones containing predominantly pelagic bioclasts including goniatites, pelagic bivalves and ostracods. Benthic elements are scarce and dominated by benthic ostracods. Millimetre-scale fenestral structures, ranging from irregular cavities to stromatactis-like forms, with micropeloidal fills at the base are abundant in the thin sections (Fig. 3). In addition, small calcite-filled microproblematica occur within the matrix as 30–50 µm oval forms or irregular elongate structures up to 500 µm in length (Fig. 3e-f).

Rocks throughout both sections contain abundant, pervasive micro-dissolution seams, oriented both parallel and oblique to bedding, commonly truncating fossils. In addition, irregular, commonly anastomosing, aluminosilicate-rich areas, from a few mm to several tens of mm in size, are present which give the limestone a nodular appearance, particularly in the Famennian parts of the sections (both red and non-red facies). Uncompacted fossils are commonly enclosed within these areas. In two instances, accumulations of bivalves and altered, yet still uncompacted, ostracod shells were observed in greater abundance in these areas than in the carbonate matrix.

Fine, subvertical, hair-like fractures filled with calcite cement locally crosscut the aluminosilicate-rich areas. Dark, ferruginous encrustations (coatings), especially on brachiopod shells, and microstromatolites are characteristic of both sections. They range from thin, irregular films without observable internal structures to thicker, laminated crusts forming oncoids with bioclasts as nuclei. These structures primarily occur in red beds but in one case were also observed in yellowish beds at Col des Tribes. They are commonly associated with microborings, particularly in formerly aragonitic shells. Encrusting agglutinated foraminifera, similar to those described by Tucker (1973), were occasionally recorded in association with these features. Finally, dark shrubby or dendritic structures resembling the problematic microfossil *Frutexites*, are present in places.

Gamma-ray spectra and mass-specific magnetic susceptibility

Data from gamma-ray spectrometry and magnetic susceptibility are shown in Table S2 (Supplementary material). The concentrations of K, U, Th and the clay gamma ray (CGR) values vary from 0.2 to 2.5% (K), from 0.2 to 4.9 ppm (U), from 0.9 to 9.5 ppm (Th), and from 8 to 78 API (CGR). The K and Th concentrations are high in the shaly F2 layers, low in the pure carbonate units (F1c) and positively correlated ($R^2 = 0.84$) indicating that both these elements are influenced by the dilution of non-radioactive $CaCO_3$. Consequently, the CGR value which is calculated from the K and Th concentrations can be considered a good indicator of shale content in the carbonates. The CGR curves (Fig. 4) show quite distinct trends of decreasing (Frasnian), increasing (lower Famennian) and again decreasing (middle Famennian) values, which are consistent with the stacking patterns of the shales and cherts (F2), strongly nodular carbonates (F1b and F1c) and weakly nodular, relatively pure carbonates (F1a). The CGR curves facilitate stratigraphic correlation between the Coumiac and Col des Tribes sections (Fig. 4). In contrast, the U concentrations are not correlated with K and Th ($R^2 = 0.13$ in both cases), and the U/Th ratios vary. Throughout the Frasnian to lower Famennian successions at both sections, the U/Th ratios are relatively low, from ~0.04 to ~0.5, regardless of the facies but they markedly increase to values between ~0.9 and ~2.1 in the LKW and UKW horizons.

The mass-specific MS values range from 1.1 to 539×10^{-7} m^3kg^{-1}; the mean value is 90.7 m^3kg^{-1} and the coefficient of variance 99.8%. The values are relatively low, with minor outliers, in the Frasnian to lower Famennian part of the sections regardless of the carbonate or shaly/cherty facies and the LKW and UKW horizons (Fig. 4). Distinctly higher MS values are observed in the lower Famennian part at both sections. In Coumiac, the MS curve partly mimic the CGR curve (Fig. 4) suggesting an influence from detrital minerals. Such patterns, however, are not visible at Col des Tribes where the MS values are markedly higher than in Coumiac, and do not correspond to the CGR curve. The correlation potential of MS is low.

Diffuse reflectance spectroscopy and colour quantification.

Data from diffuse reflectance spectroscopy are shown in Table S3 (Supplementary material). The measured colorimetric CIE*L***a***b** values range from 49.0 to 92.7 (CIE*L**), from 0.44 to 23.8 (CIE*a**) and from 5.13 to 27.3 (CIE*b**) generally indicating colours from greyscales to deep red. The yellow-band reflectance values range from 9.9 to 11.5%, the red-band values from 26.0 to 46.2%. The grey samples have a wide range of the yellow-band reflectance values but relatively low red-band reflectance whereas the two values are correlated. Samples with excess red-band reflectance over the yellow-band reflectance are red. The first derivatives of the reflectance curves are shown in Fig. 5. The grey samples (Fig. 5, top left) have distinct, broad peaks corresponding to the absorbance bands due to electron-pair transmission

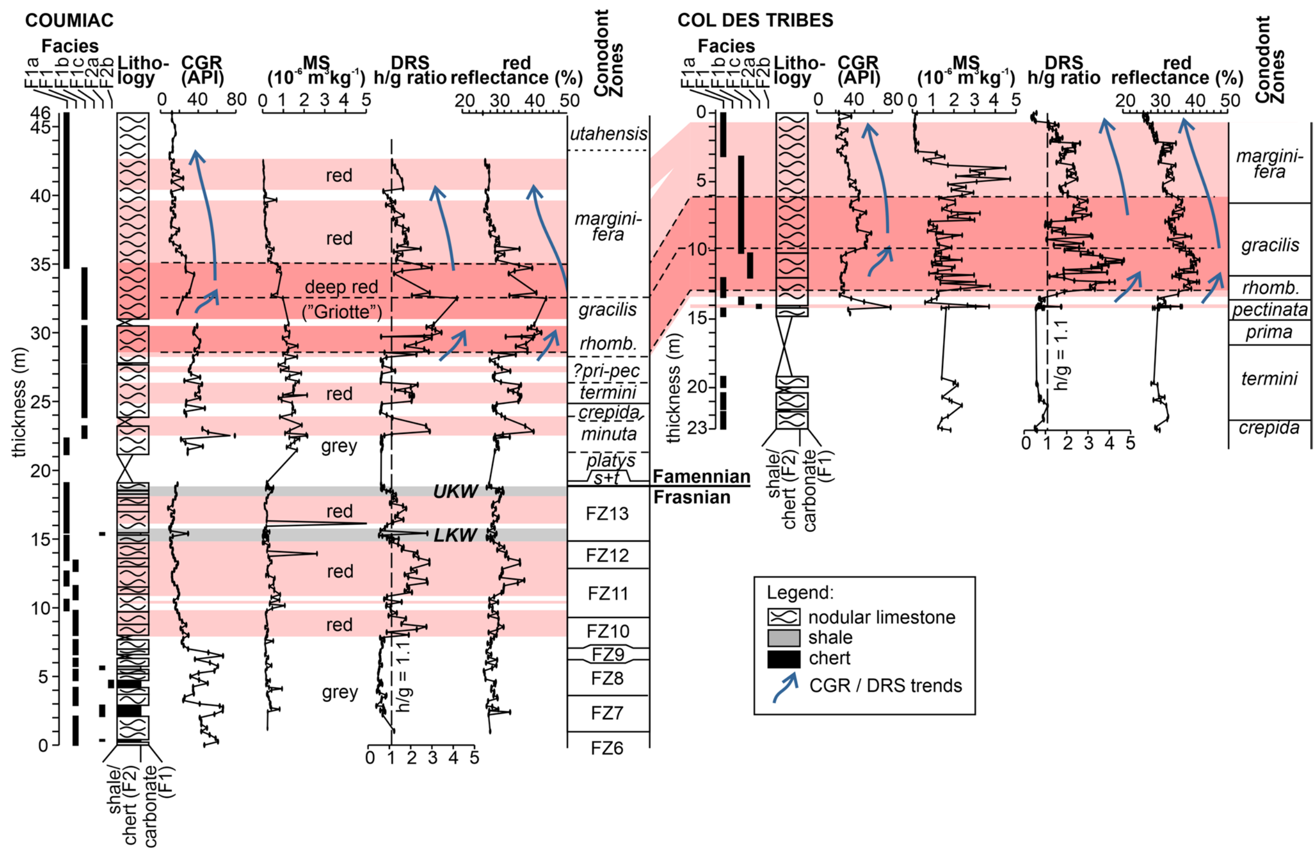

Fig. 4 Lithology, facies, conodont biostratigraphy (Klapper (1989), Klapper et al. (1993), Girard et al. (2014), and new data) and stratigraphic distribution of computed gamma-ray (CGR) data, mass-specific magnetic susceptibility (MS) and diffuse reflectance spectroscopy (DRS) data: % red-band reflectance and hematite/goethite (h/g) ratio from first derivatives reflectance curves of the Coumiac and Col des Tribes sections. Abbreviations: *s+t*—*Palmatolepis subperlobata* and *Pa. triangularis* zones, undivided; *pri*—*Pa. glabra prima* Zone; *pec*—*Pa. gl. pectinata* Zone; *rhomb.*—*Pa. rhomboidea* Zone

of goethite (425 to 445 nm and 525 to 535 nm). The deep red samples (Fig. 5, bottom right) have a prominent absorbance peak corresponding to hematite (565 to 585 nm). The samples between them show progressive reduction of both the goethite peaks and a rising prominence of the hematite peak. The ratio of peak height of hematite (565 nm) to goethite (525 nm) (hematite-to-goethite, h/g ratio) ranging from 0.35 to 4.7 is a useful proxy of the reddening due to the hematite growing at the expense of goethite. The threshold for the reddening is the starting appearance of the hematite peak at about h/g = 1.1 (Fig. 4, 5). Some rock samples in the field have black micrite or coatings that are probably Mn oxides (Fig. 2a). However, this black colour in the field was not found to have an effect on the DRS colour spectra (e.g., low CIE*L** values).

Stratigraphic distribution of the h/g ratio and the % red-band reflectance is shown in the Fig. 4. The bottom part of the Frasnian succession at both sections is non-red or just very seldom slightly reddish (Fig. 2g,h) regardless of the carbonate/siliciclastic facies (h/g values lower than 1.1). The sediment starts to redden, and the h/g ratios strongly fluctuate in the upper Frasnian and lower Famennian parts of the Coumiac section, between ~ 8 m and ~ 28 m thickness. Six major layers of red sediment, from 0.5 m to 4 m thick, are separated by slightly thinner layers of non-red sediments. Two of them correspond to the upper parts of the LKW and UKW horizons and immediately overlying strata. The higher part of the Famennian strata (Coumiac, ~ 28 m to ~ 35 m, Col des Tribes, ~ 6 to ~ 13 m) contains deep red nodular limestone of the facies F1b with high h/g ratios corresponding to the "Griotte" limestone (*Pa. rhomboidea* to *Pa. marginifera* conodont Zone). This unit is about 6 to 7 m thick, and it can be correlated well from Coumiac to Col des Tribes based on the h/g ratio, % red reflectance and the CGR values (Fig. 4).

Bulk-rock elemental composition.

The bulk-rock element concentrations from the EDXRF and ICP-MS are shown in the Table S4 (Supplementary material). The mean concentrations (μ) and coefficients of variance (CV) of major elements in the studied rocks

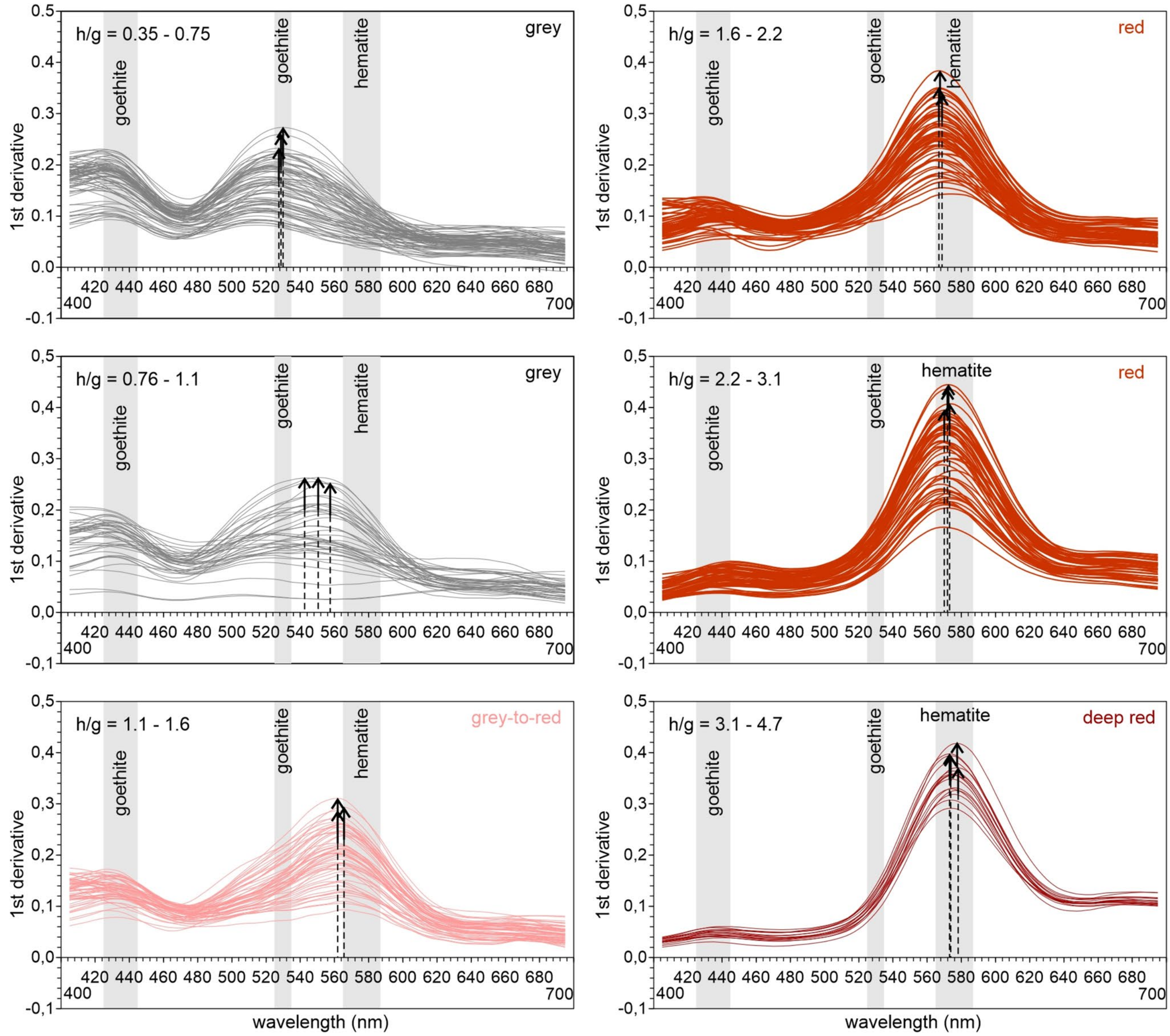

Fig. 5 First derivatives of reflectance curves of samples from the Coumiac and Col des Tribes sections. Note the increasing height of the hematite peak (565–585 nm) and decreasing height of the goethite peak (515–525 nm) with progressive reddening. The hematite-to-goethite peak height ratios increase from 0.5 (top left) to 6.5 (bottom right). Red colouration approximately starts with h/g = 1.1

are (in order of abundance): Ca (μ = 31.63%, CV = 21%), Si (μ = 3.88%, CV = 121%), Fe (μ = 2.28%, CV = 145%), P (μ = 1.11%, CV = 15%), Al (μ = 0.99%, CV = 116%), K (μ = 0.41%, CV = 107%), Mn (μ = 0.26%, CV = 122%), and Ti (μ = 0.08%, CV = 87%). The mean concentrations and CV values of trace elements are as follows: V (μ = 48 ppm %, CV = 234%), Ni (μ = 27 ppm, CV = 157%), Cu (μ = 29 ppm, CV = 207%), As (μ = 72 ppm, CV = 226%), Mo (μ = 1.4 ppm, CV = 144%), Pb (μ = 21 ppm, CV = 1122%) and U (μ = 1.3 ppm, CV = 133%). The mean concentrations of the sum of rare earth elements + Yttrium (REEY) is 70 ppm, and the CV value is 49%.

Concentrations of some elements show a distinct co-variance. Bivariate plots of element concentrations in the non-red (h/g < 1.1), pink (1.1 < h/g < 2.2) and deep red (h/g > 2.2) sediments show distinct patterns (Fig. 6). Aluminium and rubidium, typical refractory lithogenic (lithophile) elements show marked statistical correlation ($R^2 = 0.96$, Fig. 6) and so do the Al:K ($R^2 = 0.96$), Al:Ti ($R^2 = 0.9^2$) and Al:Zr ($R^2 = 0.90$). Conversely, all these elements show negative correlation with Ca (R^2 from 0.60 to 0.75). These correlations are likely driven by the dilution of phyllosilicates (clays, micas) and other clay- and silt- sized silicate minerals in calcium carbonate in the lithology range from pure carbonate to pure shale (Fig. 6). This relationship is not

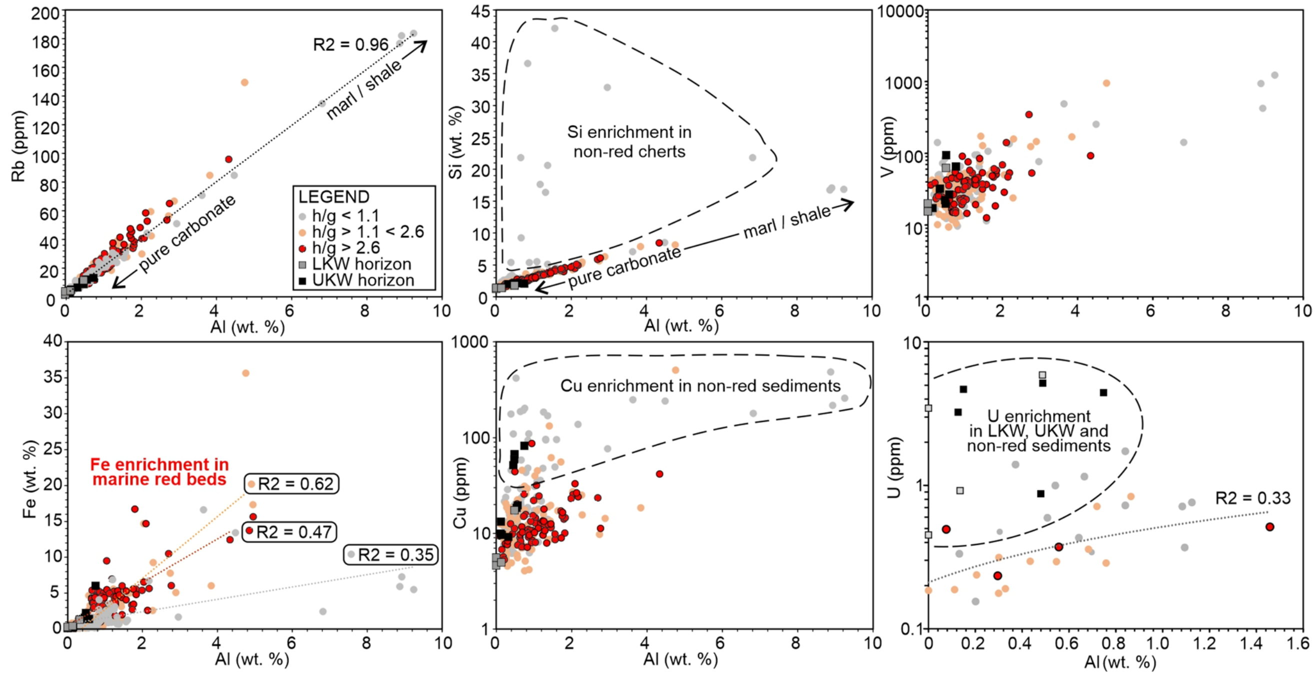

Fig. 6 Bivariate plots of selected element concentrations (EDXRF) in the red and grey sediments (indicated by values of hematite/goethite ratio, h/g, see text for explanation) of the Coumiac and Col des Tribes sections

affected by sediment colour, although the pure shales are usually non-red. The biplot of Si and Al shows two regions, a "baseline" showing a strong covariance between Si and Al due to their binding in aluminosilicate minerals in the pure carbonate – shale range, and a region of marked Si enrichment in siliceous shales and cherts, which are all exclusively non-red.

The redox sensitive elements, Fe, Mn, V, Ni, Cu, As, Mo and U show relatively high variability (high CV), little covariance with the lithogenic Al, and distributions that can be affected by the colour. Iron concentrations in the Frasnian part of the succession are relatively low (up to ~ 2.0 wt. %) and independent of the colour, but in the Famennian part, Fe concentrations are consistently higher in the red facies (in some cases very high, up to ~ 16.7 wt. %) than in the non-red facies. Concentrations of Mn show a similar distribution and relationship to red or non-red colour in the Frasnian, but they are very high (up to ~ 3.4 wt. %) in the red Griotte units (Col des Tribes, from 5.8 to 8.0 m, Fig. 7). In places, the rocks with high Mn contents contain black-coloured micrite (Fig. 2a), but the black colouration is not reflected in DRS spectra. Conversely, the concentrations of Cu, Ni and As display a wide variation across the colour range but they tend to be highest in the non-red sediments. The concentration sums of REEY are correlated with Al ($R^2 = 0.63$) in various lithologies from pure carbonate to shale and variable colour from grey to red, suggesting that bulk REEY concentrations are largely controlled by detrital and authigenic aluminosilicate admixture and not by seawater/porewater chemistry.

Positive Ce anomalies were observed in grey coloured levels with enriched redox-sensitive elements and in several deep-red coloured levels rich in Fe–Mn precipitates.

Since Rb and Al show a high dependence on the $CaCO_3$ content (see above), they were selected as suitable normalizing elements for major and trace elements to filter out the effects of changing lithology from pure carbonate to shale. However, Al, as a light element, has lower detection limits in the EDXRF analysis than the much heavier Rb. Since several samples of pure carbonates were analysed below detection limits for Al but not for Rb, the latter was chosen as a more suitable normalizing element. The stratigraphic distribution of selected element proxies normalized to Rb are shown in Fig. 7. The siliceous shales and cherts show distinct Si enrichment (Si/Rb, Coumiac, lower part). The non-red facies have high Cu/Rb, and to a lesser degree, in As/Rb, Ni/Rb and V/Rb. In contrast, Fe tends to be enriched in the red facies, most markedly in the deep-red "Griotte" facies of lower Famennian age (*Pa. rhomboidea* Zone), but also in the LKW and UKW horizons.

The LKW and UKW horizons have relatively low Al and Rb contents, comparable to the underlying and overlying strata indicating that they are developed in carbonate facies. Both the LKW and UKW show distinct enrichment in elements with affinity to reducing conditions, U (U/Th from gamma-ray spectrometry, U/Rb from ICP-MS), Cr/Rb, Cu/Rb, Ni/Rb, and V/Rb (Fig. 7). At the same time, the LKW and UKW horizons show enrichment in redox-sensitive Fe and Mn. The LKW is developed in grey carbonates whereas

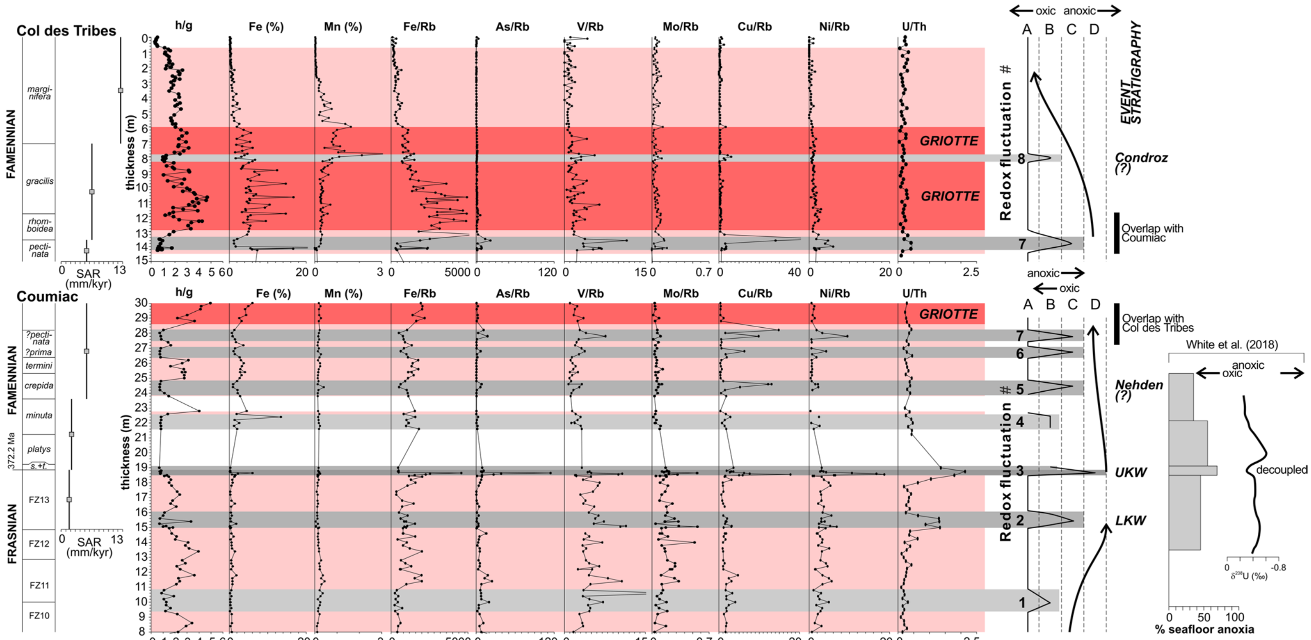

Fig. 7 Stratigraphic distribution of sediment colour (hematite/goethite, h/g ratio) and elemental redox proxies in the Frasnian/Famennian boundary interval in Coumiac and Col des Tribes, along with chronostratigraphy, sediment accumulation rates (SAR) and event stratigraphy (Lower and Upper Kellwasser Events, LKW and UKW, and an inferred position of the Nehden and Condroz Events). The redox conditions fluctuate between four modes, A, B, C, D, see text for explanation. The F/F trends in global seafloor anoxia and U isotopes from White et al. (2018) are also shown. Abbreviations: *s + t*—*Palmatolepis subperlobata* and *Pa. triangularis* zones, undivided

the UKW coincides with a transition from red to grey carbonates. The Frasnian and lower Famennian (up to the base of *Pa. rhomboidea* Zone) successions in Coumiac and also at the base of Col des Tribes show cyclic fluctuations in grey-to-red colour, associated with fluctuations in redox-sensitive Cu/Rb, Ni/Rb, As/Rb, very similar to the LKW and UKW horizons. The cycle couplets are about 3.5 m to 1.3 m thick, whereas their thickness gradually decreases from the LKW to the base of the Griotte facies. The last cycle at the base of the Griotte is a black shale (Col des Tribes, ~ 14 m).

SEM–EDX and mineralogy

SEM–EDX analyses of polished and etched thin sections revealed that the carbonate matrix in both sections consists of very finely to finely crystalline $CaCO_3$ crystals ranging from < 5 µm to ~ 30 µm in size, thus classifying them as micrite and microspar. The crystals were commonly pitted, with many empty pits exhibiting regular rectangular shapes (Fig. 8a) and displaying sharp contacts with adjacent bioclasts. The irregular aluminosilicate-rich areas, visible under optical microscope, contain dense accumulations of fine-grained filamentous, vermicular, and lath-like K-Fe-Mg aluminosilicates. The lath-like types appear to be dispersed in both the aluminosilicate matrix and surrounding carbonate framework, and they are considerably less abundant than the filamentous aluminosilicates. In addition, the aluminosilicate areas contain µm-scale Mn oxides and anhedral to subhedral iron oxides, Ti oxides, euhedral to anhedral F-apatite, and quartz grains with apatite inclusions. The contacts between these areas and surrounding carbonate are sharp or gradual (Fig. 8b–c). The filamentous aluminosilicates are commonly associated with euhedral to subhedral quartz grains up to 25 µm in size. Complex intergrowths are common, including lath-like aluminosilicate inclusions within the quartz crystals (Fig. 8d). Gradational transitions between the aluminosilicate and quartz commonly occur (Fig. 8e).

In the red facies, these filamentous and vermicular aluminosilicates in the carbonate matrix and aluminosilicate-rich areas contain clusters of submicron platelets and needle-like iron oxides, with common transitions between these two phases (Fig. 8b–c, f–h, Fig. 9). The Fe-oxide-rich clusters are enriched in Fe and depleted in Si, Al and K in the elemental distribution maps (Fig. 9). The lath-shaped aluminosilicates, although present in both the matrix and the areas, do not occur in association with these submicron iron oxides (Fig. 8f). In non-red beds, the submicron Fe oxides are missing, but there are bigger, anhedral and euhedral Fe oxide grains associated with aluminosilicates and Fe-oxide pseudomorphs after pyrite framboids (Fig. 8i–j), both displaying residual sulphur in the EDX spectra. Locally, carbonaceous matter occurs within the masses of aluminosilicates via a high C-peak in the EDX spectra in the non-red facies.

In the red facies, the K-Fe–Mg aluminosilicates occur in association with microstromatolitic structures overgrowing skeletal grains (Fig. 8g-h) and thin, irregular ferruginous coatings and oncoids (Fig. 8k–l), all containing submicron grains of Fe oxides (Fig. 8h-i,l). These ferruginous coatings display distinct microlamination and contain euhedral and subhedral fluorapatite, other authigenic minerals and abundant carbonaceous matter (Fig. 8k–l), indicated by high carbon peaks in the EDX spectra. In places, the (originally aragonitic?) shells are replaced by needle-like Mn oxides that tend to penetrate into the microstromatolitic encrustations indicating that they grew during or after the microstromatolite growth (Fig. 8h-i). In places, agglutinated foraminifera are incorporated in the coatings. In addition, the aluminosilicates replace $CaCO_3$ of the shells of both originally aragonitic (goniatites) and calcitic taxa (dacryoconarids) and they are also present in the shell microborings. The microborings contain abundant organic matter, Si, Al, K and Mg associated with filamentous aluminosilicates and submicron-sized Fe- and locally Mn oxide grains.

The observed K-Fe–Mg aluminosilicates generally show similar major element compositions (Table S5, Supplementary material; Figs. 9, 10). All phases are systematically K-rich, with varying Mg and Fe content, the latter being influenced in red beds by submicron-sized iron oxides. The EDX analyses revealed Si/Al ratios calculated from oxide weight percentages ranging from 1.27 to 3.87 (median 1.81, n = 68). These ratios, combined with their diagnostic morphologies (lath-like, filamentous and vermicular), are consistent with the clay mineral phases. However, specific clay mineral identification was not attempted without complementary XRD analyses. The filamentous aluminosilicate phases are commonly enriched in Fe oxides (up to 67 wt. %), but the lath-shaped phases are not (Fig. 10).

In-situ element geochemistry (LA-ICP-MS).

The LA-ICP-MS data are shown in Table S6, Supplementary material. There is a distinct chemical variability across different colours, textures and components on the micro-scale (Tab. 1). The microspar matrix has highly variable contents of Al (from 1 ppm to 4.8%) and Ca (from 25.4 to 39.9%) which are negatively correlated ($R^2 = 0.88$). Aluminium in the microspar is positively correlated with Si ($R^2 = 0.72$), Ti ($R^2 = 0.9$), Th ($R^2 = 0.72$) and other elements suggesting that the microspar is a mixture of calcite and aluminosilicates, mainly clay minerals. The Al-normalized, redox sensitive elements show distinct colour-related trends (Fig. 11). The contents of Fe and V (Fe/Al and V/Al) markedly increase from the grey towards the red microspar whereas As/Al, Cu/Al and U/Al show opposite trends. The grey-to-red colour change is also accompanied by a progressive decrease in Si/Al ratios by about 25%. Manganese and molybdenum do not show any colour-related trends, but both these elements plus Cu, Ni, Co and Fe are enriched in the black fine-grained matrix between the nodules in the deep red "Griotte" facies in the Col des Tribes section (Fig. 11). The high Mn contents (up to 7.5%) and black colour suggest the presence of Mn oxide minerals in the matrix.

Biogenic and early diagenetic features in the studied samples are represented by the laminated encrustations on brachiopod shells, dark shrubby or dendritic structures (*Frutexites*), and microborings of brachiopod shells (see Sect. Minerals associated with early diagenesis). The microborings and encrustations have variable contents of Ca (from 7. to 39%), higher Al contents than the micrite and they feature a weak negative correlation between Al and Ca ($R^2 = 0.53$) and positive correlation between Al and Ti ($R^2 = 0.87$) suggesting that they contain aluminosilicate minerals. These structures show variable, in places very high enrichment in Fe, V, Ni, Co, Mo and U (Tab. 1).

The sums of REEY contents range from 0.8 to 305 ppm with the mean, m = 76.2 ppm, and CV = 80.5%. The sum REEY from the analytical spots fail to show any correlation with Al ($R^2 < 0.1$), which is in marked contrast with the bulk-rock REEY data that are well correlated with Al. This indicates that some REE fractionation occurs on the micro-scale but not on the bulk-rock scale. The UCC-normalized REEY patterns from the LA-ICP-MS are shown in Supplementary material (Fig. S1). The REEY of grey micrite, the *Frutexites* microproblematica and microborings have relatively flat patterns, with minor middle REE bulge. With progressive colouration from yellow to red, the micrite REEY tend to be depleted in light REE and show fluctuating, positive or negative Ce anomaly.

Discussion

Interpretation of depositional environment.

The environmental interpretations of the sections are based on mud-dominated lithologies, and the predominance of nektonic and planktic bioclasts (goniatites, styliolinids, radiolarians, pelagic ostracods and bivalves) over benthic ones. In places, the rocks contain blind and reduced-eye trilobites (*Nephranops*, *Tripholiops*, *Dianops*, *Chaunoproetus*, *Calybole*) and deep-water bivalves (*Guerichia*) (Girard et al. 2014). Conodont assemblages in the Famennian part (Col des Tribes section) are dominated by pelagic genus *Palmatolepis* and *Bispathodus*, and low percentages (<25%) of the more shallow-water icriodid and polygnathid taxa. These features indicate deposition in low-energy conditions well below storm-wave base, below the photic zone,

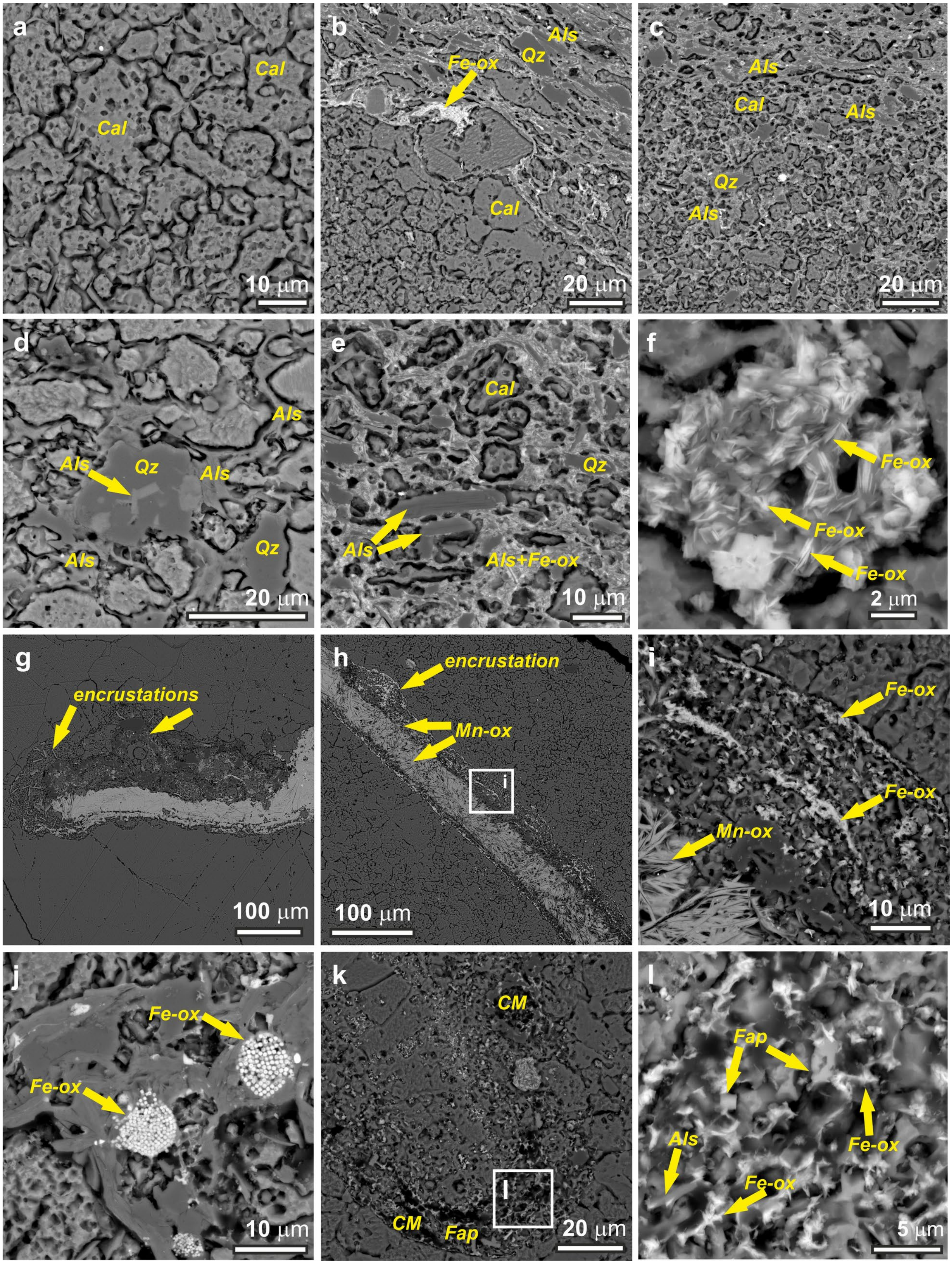
a
Cal
Cal
10 µm
b
Als
Qz
Fe-ox
Cal
20 µm
c
Als
Cal
Als
Qz
Als
20 µm
d
Als
Als
Qz
Als
Qz
Als
20 µm
e
Cal
Qz
Als
Als+Fe-ox
10 µm
f
Fe-ox
Fe-ox
Fe-ox
2 µm
g
encrustations
100 µm
h
encrustation
Mn-ox
i
100 µm
i
Fe-ox
Fe-ox
Mn-ox
10 µm
j
Fe-ox
Fe-ox
10 µm
k
CM
l
CM
Fap
20 µm
l
Fap
Als
Fe-ox
Fe-ox
5 µm

Fig. 8 Backscattered electron (BSE) images: (**a**) microsparitic matrix with pitted calcite (Cal) crystals; the pits are interpreted as voids after dissolved aragonite, following the model of Munnecke et al. (1997), non-red facies, Col des Tribes, sample CO 0; (**b-c**) aluminosilicate-rich areas with sharp (**b**) and transitional (**c**) boundaries with microsparitic matrix; the areas comprise quartz (Qz) and aluminosilicate (Als) matrix with associated submicron-sized iron oxides (Fe-ox) and quartz grains, red facies, Col des Tribes, sample CO 6.9; (**d**) filamentous and vermicular K-Fe–Mg aluminosilicates within the microspar framework; note aluminosilicate inclusions within quartz, and gradual transitions between aluminosilicate and quartz phases, non-red facies, Coumiac, sample CC 6.7; (**e**) aluminosilicate-rich area in red limestone, Col des Tribes, sample CO 7.23; note two Fe-oxide-free aluminosilicate laths (arrows) with well-delimited grain boundaries floating within a matrix of aluminosilicates associated with Fe-oxides (Fe-ox); (**f**) detail of K-Fe–Mg aluminosilicate-rich area with submicron-sized, needle-like Fe oxides (Fe-ox), red facies, Coumiac, sample CC 15.7; (**g,h,i**) two examples and one detail (i: enlarged frame in h) of microbial encrustations around skeletal grains composed of calcite, aluminosilicates and Fe-oxides (arrows), note that the shell (originally aragonite?) is replaced by needle-like Mn-oxides (h,i, arrows), Col des Tribes, sample CO 6.9; (**j**) aluminosilicate-rich area in non-red facies composed of K-Fe–Mg aluminosilicates with Fe-oxide pseudomorphs after framboidal pyrite (arrows), Col des Tribes, sample CO 6.9; (**k-l**) ferruginous oncoids with a cortex composed of submicron-sized Fe oxides, dark carbonaceous matter (CM), authigenic fluorapatite (Fap) and K-Fe–Mg aluminosilicates within the carbonaceous framework, red facies, Col des Tribes, sample CO 6.9 (l: enlarged frame in k)

in an outer ramp setting at depths from several tens to several hundred metres (Tucker 1975; Préat et al. 1998, 1999; Devleeschouwer 1999; Girard et al. 2014). Sparse benthic assemblages dominated by tolerant ostracods reflect oxygen-depleted conditions, whereas bioturbation (evidenced by the lack of lamination in carbonates) indicates infaunal activity. Generally, there is a lack of sedimentary structures indicating significant hydrodynamic activity, with the exception of the F1b subfacies (Griotte limestone) containing size-sorted goniatites, and abundant condensed horizons and hardgrounds indicating weak current activity (Girard et al. 2014). Sharp-based skeletal accumulations of crinoids (Fig. 2f) and current-oriented dacryoconarid accumulations occur in the Frasnian succession of Coumiac indicating that pelagic sedimentation was punctuated by storms or gravity flows (Préat et al. 1998). Both Préat et al. (1998) and Girard et al. (2014) suggested that sedimentation was affected by six significant eustatic fluctuations in Coumiac (predominantly Frasnian) and seven fluctuations in Col des Tribes (predominantly Famennian).

Minerals associated with early diagenesis.

The observed pitted texture of the carbonate matrix (Fig. 8a) closely resembles the features described by Lasemi and Sandberg (1984) and Munnecke et al. (1997) who interpreted the pits as moulds of dissolved aragonite needles and needle bundles. The absence of calcite crystal alignment and flattening indicates that the microspar precipitation occurred very early during diagenesis, which is consistent with previous interpretations of the Griotte facies by Tucker (1975). Therefore, the matrix is interpreted as early diagenetic, very shallow-burial marine cement (microspar) that replaced original aragonite-rich mud (Munnecke et al. 1997). The early-diagenetic aragonite dissolution in low-energy carbonate environments is driven by bacterial decay of organic matter (Munnecke et al. 2023).

The filamentous and vermicular morphology of the K-Fe–Mg aluminosilicates present in the carbonate framework and aluminosilicate-rich areas, and their intergrowth patterns with quartz grains (Fig. 8b-e) indicate an authigenic origin of the clays. Although textural evidence suggests neoformation from silica-rich fluids, transformation processes may also have been involved. In contrast, grain size, morphology and sharp grain boundaries of the lath-shaped aluminosilicates present in the matrix and the aluminosilicate-rich areas suggest their detrital origin (Fig. 8f). The lath-shaped aluminosilicates are considerably less abundant than the filamentous forms, suggesting that authigenic phases predominate. This is consistent with the conclusions of Devleeschouwer (1999), who reported predominantly K-rich phyllosilicates (illite) with low crystallinity from the Coumiac section and interpreted their low mineralogical diversity as evidence of an authigenic origin through diagenetic transformation. The clay mineral authigenesis within the aluminosilicate-rich areas and the surrounding microspar occurred most likely during early diagenesis, shortly after the microspar crystallization. These areas likely acted as localized pathways for early diagenetic fluids, promoting dissolution–precipitation reactions, and the K-Fe–Mg aluminosilicate authigenesis (cf. Evans and Elmore 2006). Locally, in non-red beds, carbonaceous (organic) matter occurs within the aluminosilicate masses (Fig. 8j), and this could have played a role in the mediation of clay mineral authigenesis (Vodrážková et al. 2025). The aluminosilicates may have formed through organomineralization of microbial organic matter (Vodrážková et al. 2025) within ferruginous crusts and microstromatolitic encrustations on bioclasts (Fig. 8k–l; Fig. 10). Alternatively, the authigenic aluminosilicates within microspar and aluminosilicate-rich areas may have formed during or shortly after the microspar crystallization (Figs. 8b-c,f–h; 9).

Sediment reddening, hematitization and its possible microbial and abiotic pathways.

In the red facies, abundant submicron-sized Fe-oxides occur within the microstromatolitic bioclast encrustations and microborings, which indicate their very early diagenetic origin. The submicron hematite pigment is a common feature of marine red beds throughout the Phanerozoic (Cai et al.

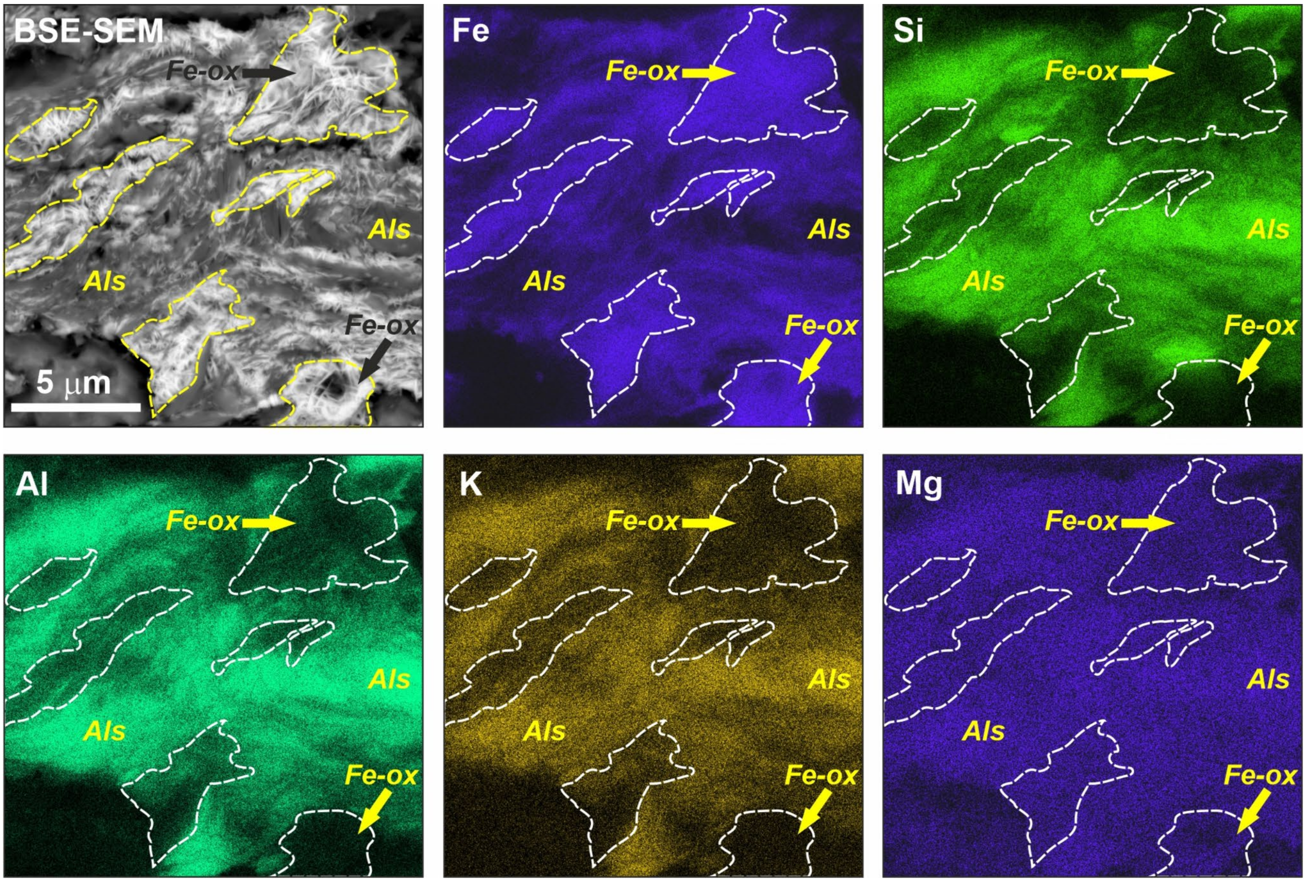

Fig. 9 SEM–EDX elemental mapping of authigenic aluminosilicate assemblage within a dissolution seam; sample CC 10, red facies; backscattered electron (BSE, top left) image showing filamentous aluminosilicate textures with clusters (dashed lines) of submicron platelets of Fe oxides, and corresponding elemental distribution maps for Fe, Si, Al, K, and Mg. Note the enrichment in Fe and depletion in Si, Al, and K of the Fe-oxide clusters, as well as Fe occurring both as a structural component of clay minerals (diffuse distribution) and as discrete submicron oxide phases (bright patches in BSE image)

2012; Hu et al. 2012; Bábek et al. 2021). The morphology and microstromatolitic structure of the ferruginous coatings on bioclasts (encrustations), the presence of agglutinated foraminifers within the coatings, and the presence of carbonaceous matter and authigenic fluorapatite (Fig. 8k-l) all indicate that hematite precipitation was associated with microbial colonization and biofilm formation (Vodrážková et al. 2022, and references therein). Préat et al. (1999) and Mamet and Préat (2006) attributed the red colouration to the activity of microaerophilic iron-oxidizing bacteria that precipitated submicron Fe oxides within microbial structures at the Coumiac section. Microstromatolites and microborings with clay minerals and submicron hematite were reported from MRBs from the lower Devonian of the Prague Basin, Czechia, middle-upper Ordovician of the Yangtze Platform, South China, and Jurassic, Italy (Préat et al. 2008, 2018; Bábek et al. 2021, 2022). Direct microscopic evidence of microbe preservation is missing in our material. However, evidence of morphologically well-preserved microbial communities occurring in direct association with iron oxyhydroxide precipitates is not common, although there are examples from both present-day environments (Hanert 2002) and ancient stromatolites (Lozano and Rossi 2012). Various pathways for microbial precipitation of hematite and Fe oxyhydroxides (hematite precursors) have been described including precipitation by anaerobic or microaerophilic Fe-oxidizing bacteria (Widdel et al. 1993; Emerson and Revsbech 1994; Straub et al. 1996), and microbially mediated ion attraction by negatively charged cell surfaces and extracellular polymeric substances (EPS) (Fortin et al. 1998; Konhauser et al. 1993; Préat et al. 1999, 2008). Another possible pathway is the reduction–oxidation cycling involving coupled communities of iron-reducing and iron-oxidizing bacteria utilizing structural iron in mineral phases (e.g., Cooper et al. 2020).

Submicron Fe-oxides are also closely associated with the authigenic filamentous and vermicular aluminosilicates within the carbonate matrix and in the aluminosilicate-rich areas (Fig. 8b-c, f–h; Fig. 9). These structures likely formed during and/or shortly after the microspar growth but

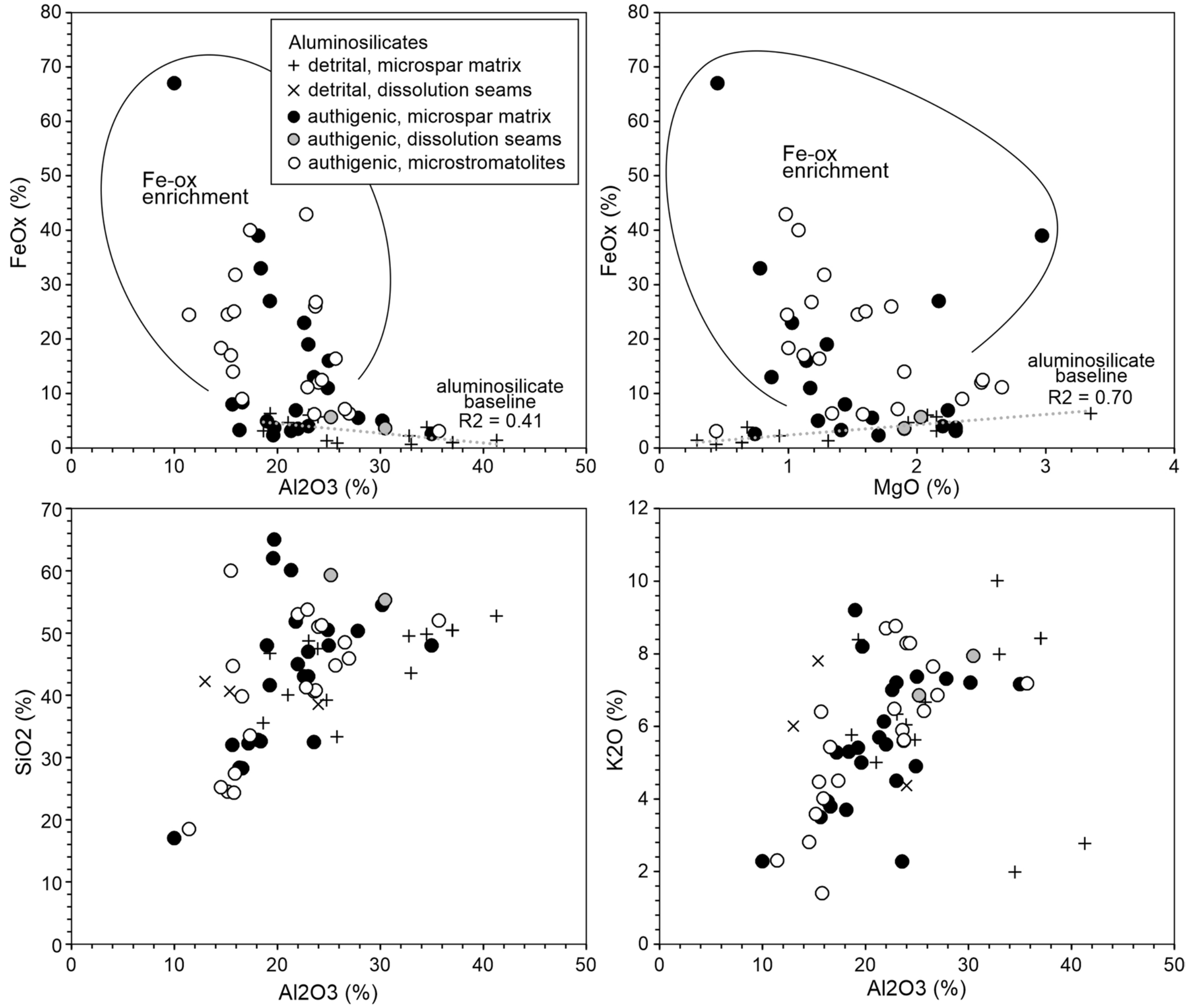

Fig. 10 Bivariate plots of element concentrations from EDX-SEM spot analyses of various types of lath-like (detrital) and filamentous + vermicular (authigenic) aluminosilicates. Note the significant enrichment in Fe (up to 67 wt% of Fe-oxides) in the authigenic phases, which is missing in the detrital ones. In contrast, the detrital and authigenic phases have similar SiO2/Al2O3 and K2O/Al2O3 ratios

preceded the formation of microfractures during burial diagenesis. This may suggest additional mechanisms of hematite precipitation. The Fe oxides may have developed from Fe-bearing aluminosilicates formed during organomineralization whereby degradation of microbial organic matter provided the chemical precursors for clay neoformation (Vodrážková et al. 2025). The Fe^{2+} release from clay minerals and subsequent precipitation of hematite (or Fe oxyhydroxides as hematite precursors) in MRBs was assumed to result from microbial Fe^{2+}–Fe^{3+} cycling along redox gradients (Bábek et al. 2021; Vodrážková et al. 2022). Redox gradients form most easily in the shallow sediment subsurface on seafloor (Fig. 12), due to microbial oxidation (respiration) of organic matter present in the sediment. The water column above the bottom represents an external source of oxygen as the most favourable electron acceptor for the oxidation (Orsi 2018). The thickness of the redox boundary and its depth below the sediment–water interface is dependent on many variables including the supply of organic matter, sedimentation rates, O_2 content in water column, grain size and permeability of the sediment and the rate of microbial decomposition of microbial communities living below the sediment–water interface (Bábek et al. 2021; Munnecke et al. 2023, their Fig. 4).

The co-occurrence of authigenic hematite with authigenic clay minerals (Fig. 9b-c, f–h, Fig. 10) requires consideration of abiotic pathways for the Fe oxyhydroxide precipitation. They include: (i) sorption of Fe^{2+} onto clay mineral surfaces followed by oxidation in the presence of oxidizing fluids, a mechanism which is also applicable to

Table 1 Mean values and ranges of concentrations of selected elements in various carbonate components point-analysed by Laser-Ablation mass spectrometry with inductively coupled plasma (LA-ICP-MS)

Component		Al	Si	Ca	V	Mn	Fe	Ni	Cu	As	Mo	Ba	U	REEY
		(%)	(%)	(%)	ppm	(%)	(%)	ppm	ppm	ppm	ppm	ppm	ppm	ppm
Grey	Mean	0.43	1.35	37.85	6	0.12	0.37	3	11	213	0.1	15	0.2	59
Microspar	Min–max	0.03–0.86	0.03–5.41	33.58–39.37	3–12	0.01–0.28	0.16–1.02	1–6	1–53	1–1665	0.0–0.4	3–33	0.1–0.4	18–179
Yellow	Mean	0.61	1.95	36.71	15	0.35	0.92	14	18	126	0.3	49	0.3	81
Microspar	Min–max	0.00–3.77	0.13–8.19	25.38–39.54	0–70	0.04–1.66	0.06–5.20	3–148	1–148	1–1045	0.0–3.6	1–387	0.0–2.0	5–305
Pink	Mean	0.31	0.75	38.33	6	0.07	0.24	4	7	32	0.1	11	0.1	48
Microspar	Min–max	0.05–0.88	0.09–1.92	35.65–39.52	1–13	0.01–0.14	0.06–0.55	1–8	0–27	1–69	0.1–0.4	2–25	0.0–0.4	7–274
Red	Mean	0.52	1.05	37.85	18	0.16	0.94	11	2	21	0.1	18	0.2	59
Microspar	Min–max	0.00–4.78	0.01–6.28	27.52–39.93	0–196	0.04–1.10	0.02–6.10	2–96	0–12	1–248	0.0–1.0	0–175	0.0–1.1	5–232
Mn crust	Mean	0.88	1.87	32.27	24	7.19	1.86	63	79	36	3.1	141	0.2	68
	Min–max	0.68–1.08	1.74–2.00	32.02–32.53	19–29	6.87–7.52	1.62–2.10	55–71	76–82	35–36	2.9–3.3	112–170	0.2–0.2	61–75
Frutexites	Mean	0.53	6.03	33.21	29	0.31	1.45	14	40	24	0.1	30	0.8	149
	Min–max	0.17–1.43	0.35–33.80	7.67–38.76	10–90	0.04–0.57	0.55–3.63	4–63	4–177	6–84	0.1–0.3	8–97	0.3–3.3	41–191
Micro-	Mean	3.43	8.66	21.91	233	0.24	13.05	52	5	134	1.3	46	1.6	150
borings	Min–max	0.13–5.86	0.01–17.32	9.92–38.74	12–404	0.06–0.90	0.92–21.60	10–78	0–14	32–247	0.2–2.2	4–94	0.1–2.7	32–263
Micro-stromatolite	Mean	1.16	3.45	34.48	46	0.23	2.16	28	4	61	0.3	36	0.6	77
	Min–max	0.10–6.37	0.09–14.18	25.85–39.38	3–173	0.09–1.03	0.11–8.63	2–130	0–21	1–262	0.0–2.4	4–224	0.1–6.8	24–216

Mn oxides (Van Groeningen et al. 2020; 2021); (ii) electron transfer from adsorbed Fe^{2+} to structural Fe^{3+} within the clay mineral lattices, producing Fe^{3+} minerals without molecular oxygen (Gorski et al. 2012; Schaefer et al. 2011), and (iii) clay mineral transformations (e.g., illitization) that release structurally bound Fe^{2+} and Fe^{3+} ions (Środoń et al. 1992; Stirrat et al. 2017). In this last process, the final mineral products are controlled by redox conditions, forming pyrite under reducing- and Fe oxides under oxidizing conditions. In our material, this mechanism may explain the difference between the red facies containing Fe-oxide-bearing aluminosilicates, and non-red ones containing the same authigenic clays without submicron Fe oxides, and Fe-oxide pseudomorphs after pyrite and pyrite framboids (Fig. 8i-j).

Importantly, the submicron Fe oxides were observed exclusively in association with authigenic clay minerals, but not with the detrital ones. This observation may reflect the relatively higher specific surface areas and higher chemical reactivity of the authigenic phases compared to detrital phases (Steiner et al. 2022; Kang et al. 2024). These parameters increase their capacity to adsorb Fe^{2+} and promote the nucleation of Fe^{3+} oxides. The highly reactive authigenic aluminosilicates might represent primary substrates for Fe oxide precipitation during early diagenesis of the MRBs.

Geochemical expression of the redox-driven colour changes.

The red and non-red sediments show contrasting concentrations of redox-sensitive elements V, Mo, As, Cu and U, both on mesoscopic (bulk-rock EDXRF and ICP-MS) and microscopic (*in-situ* LA-ICP-MS) scales (Figs. 6, 7, 10; Table 1). Species of these elements with higher valency (e.g., uranyl ion, UO_2^{2+}, vanadyl ion VO^{2+}, and other) generally form soluble complexes in oxygenated sea-water. When reduced, they are scavenged and transferred into solid form through organic matter remineralization and/or precipitation of carbonates, Fe/Mn oxyhydroxides, pyrite and diagenetic clay minerals (Rudnicki and Elderfield 1993; Tribovillard et al. 2006; Smrzka et al. 2019). Below the sediment–water interface, these elements may be further dissolved and fixed to solid matter due to redox reactions between the minerals, organic matter and pore water (Morford and Emerson 1999; Morford et al. 2005; Smrzka et al. 2019). Redox-driven dissolution–precipitation of Fe/Mn oxyhydroxides ("particulate shuttle") may play a critical role in redistribution of the redox-sensitive elements (Algeo and Tribovillard 2009; Algeo and Li 2020). This elemental cycling is strongly dependent on the redox gradients that may develop above or below the sediment – water interface. The gradual enrichment in early diagenetic Fe(III)-bearing hematite from the grey through to yellow, pink and red microspar in the red

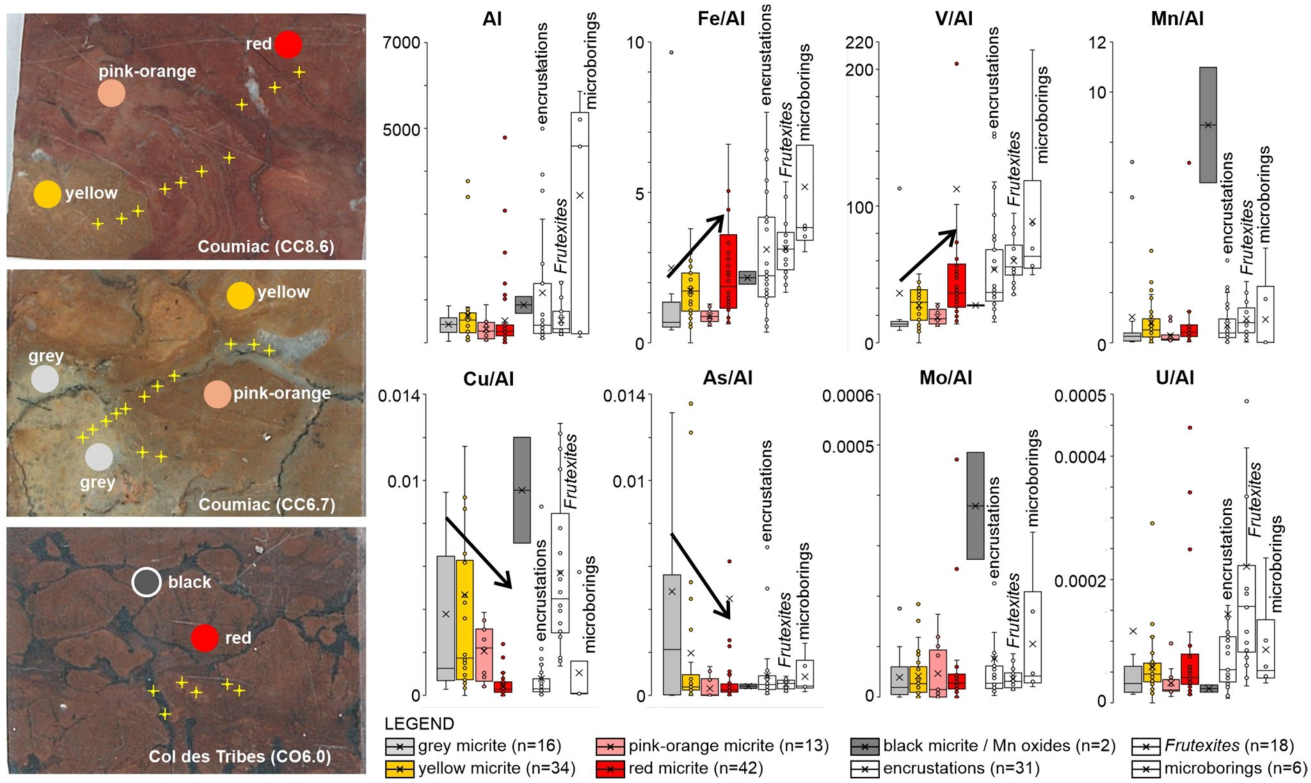

Fig. 11 Laser ablation inductively coupled plasma mass spectrometry (LA-ICP-MS) data from various components of the studied rocks: (**a**) polished slabs showing micrite with variable colour: grey, yellow, orange-pink, red and black; (**b**) boxplots showing Al contents, and Al-normalized element ratios of the main components, coloured micrite, encrustations on brachiopod shells, *Frutexites* microproblematica and microborings in brachiopod shells. For better visibility of the boxes, far-outliers are not depicted

facies is coupled with progressive increase in total Fe, V and Fe/Al and V/Al ratios and gradual decrease in total Cu, As and Cu/Al and As/Al ratios (Fig. 11, Table 1). This coupled geochemical and colour progression suggests a shift towards more oxic conditions. The microbial structures (microstromatolites, *Frutexites* and microborings) show ever increasing total Fe and Mn concentrations, Fe/Al and Mn/Al ratios, and they have higher and variable V/Al, Cu/Al, Ni/Al, Mo/Al and U/Al ratios (Table 1, Fig. 11). This underscores the role of Fe/Mn oxyhydroxides (particulate shuttle) in trace element scavenging under variable micro-redox conditions.

The UCC-normalised REEY patterns demonstrate that the redox variations are greater on a micro-scale (<1 mm) than on the macro-scale (>10 cm). The Ce anomalies in REEY patterns are used as palaeoredox indicators in view of oxidative fixation of soluble Ce(III) to sediment-fixed Ce(IV) (German and Elderfield 1990). The microscopic REEY distributions show progressive development of both positive and negative Ce/Ce* anomalies on the transition from grey to red micrite, and in the encrustations (Fig. S1b,c,e,f,h) reflecting redox fluctuations. However, the bulk-rock REEY patterns are similar in the grey and red facies, showing only weak negative Ce anomalies (Fig. S1a,d,g). In addition, the sum of REEY is correlated with Al in bulk-rock samples suggesting a predominant detrital control (Della Porta et al. 2015), whereas this correlation is lacking on the micro-scale, suggesting a greater role of hydrogenic REEY fractionation. The *in-situ* geochemical patterns support our previous assumptions from petrographic observations that the hematite precipitated *within* the sediment, in the shallow sediment subsurface, and was accompanied by elemental redox-cycling on micro (mm) scales.

Redox stratigraphy of the Frasnian-Famennian boundary interval.

The successions at both studied sections are condensed, as demonstrated by fragmentary preservation of skeletal grains and abundant shell hash which resulted from prolonged seafloor exposure and bioturbation rather than current transport. The bottom exposure and slow sedimentation rates are supported by the presence hardgrounds, ferruginous crusts and encrusting agglutinated foraminifera on skeletal grains. The thickness of the conodont zones at the sections (Klapper et al. 1993; Girard et al. 2014) and their duration inferred from the Geological Time Scale 2012 (Becker et al. 2012) yield average sediment accumulation rates (SAR) from ~1.7 mm/kyr in the latest Frasnian (Upper *Pa. gigas*

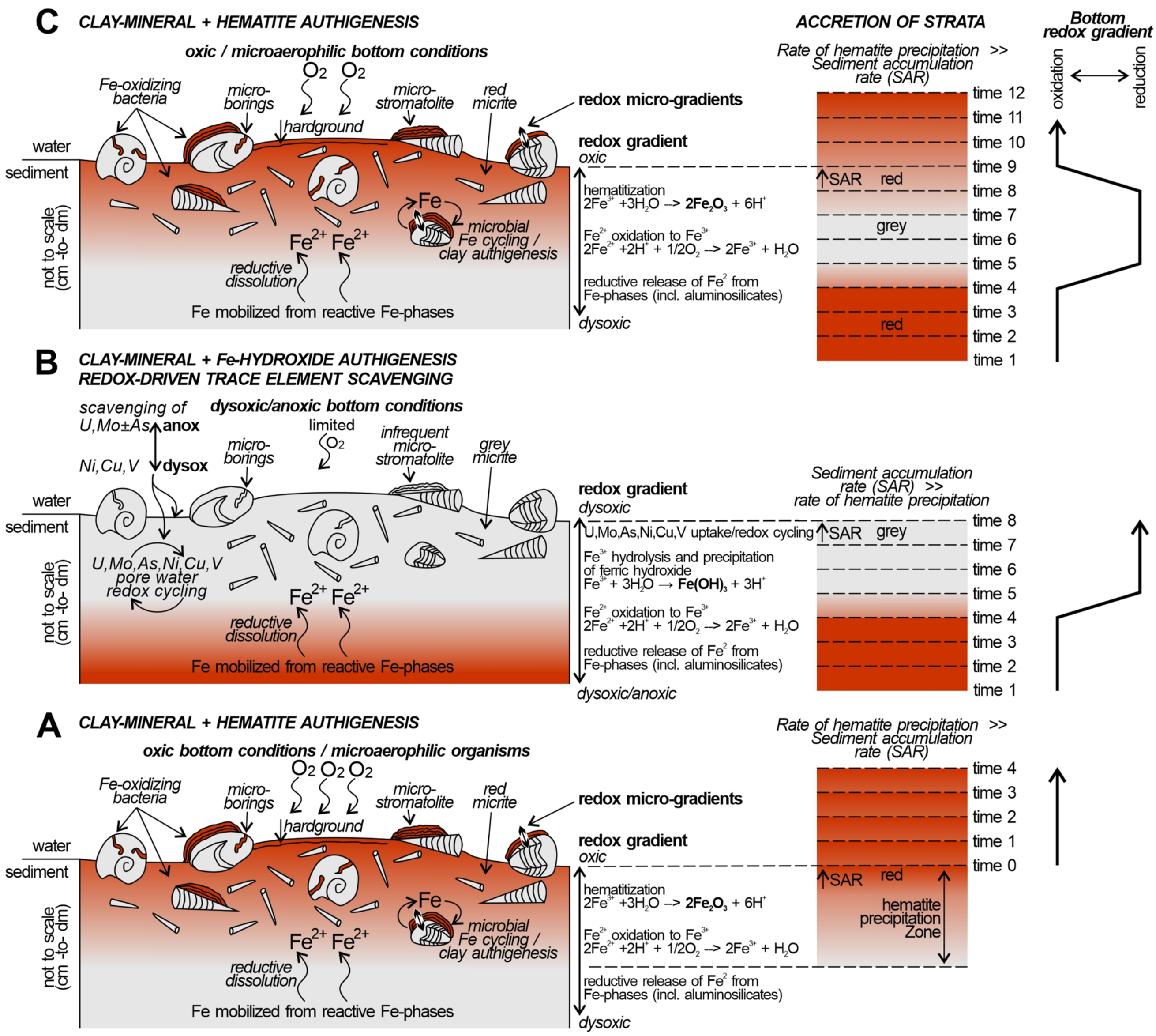

Fig. 12 Conceptual model of early diagenetic hematitization under oxic bottom water conditions (**A, C**) and development of a grey layer during dysoxic-anoxic bottom water conditions (**B**) representing one of the redox cycles discussed in the text

– *Pa. linguiformis* Zones, FZ10-13) to ~ 12.7 mm/kyr in the Famennian (*Pa. marginifera* Zone) (Fig. 7). Up-section the SAR gradually increase. These SAR values are comparable to other Phanerozoic examples of MRBs, which range from ~ 2 mm to ~ 26 mm/kyr (Wang et al. 2005; Jansa and Hu 2009; Bábek et al. 2021). Combined with water column oligotrophy and oxic bottom conditions the low SARs seem to be the prerequisites for deposition of MRBs (Franke and Paul 1980; Wang et al. 2005; Hu et al. 2012; Bábek et al. 2018). The low limit of the SARs approaches the accumulation rates of modern pelagic red clays (about ~ 0.5 mm/kyr) (Gleason et al. 2002).

In the interval from the late Frasnian (FZ12) to the *Pa. rhomboidea* Zone spanning about 9 Myr (Becker et al. 2012, their Fig. 22.12), the red successions in Coumiac and Col des Tribes feature at least eight distinct stratigraphic horizons (redox fluctuation cycles 1–8, Fig. 7), including the Lower and Upper Kellwasser Horizons. These horizons have a non-red colour and elevated concentrations of redox-sensitive elements, As, V, Mo, Cu, Ni and U (Fig. 12). The cycle #7 (*Pa. gl. pectinata* Zone) located 27.5–28.2 m in Coumiac can be correlated with the level at 13.3–14.2 m in Col des Tribes based on common colour and geochemical characteristics providing a tie link between the two sections (Fig. 7). The redox horizons are ~ 0.5 to ~ 1.5 m thick, each representing approximately 77 to 590 kyr of time span including the LKW and UKW, calculated using the SAR values given in Fig. 7. This is within the time constraints of the LKW and UKW horizons in the Steinbruch Schmidt section, Germany, which were calibrated to astrochronology cyclicity giving durations of 90 and 110 kyr, respectively (Da Silva et al. 2020). The red horizons between the cycles are thicker, representing longer time intervals roughly from 770 (*Pa. rhomboidea* Zone) to 1,440 kyr (interval between the LKW and UKW), which is beyond the time limits of about 470 kyr calculated by Da Silva et al. (2020).

The geochemical characteristics indicate that the sedimentary system fluctuated between two end-member redox modes: mode A represented by the red limestones with elevated hematite concentrations and Fe/Rb ratios reflecting oxic conditions, and mode D represented by non-red limestones/marls of the UKW with distinctly elevated concentrations of U, Ni, Cu, Mo, V and As (redox cycle 3) reflecting anoxic conditions (Figs. 7, 12). The geochemical signature of the UKW is assumed to reflect peak anoxic conditions consistently with the widespread interpretation of the F/F biotic crisis (Buggisch 1991; Joachimski and Buggisch 1993; Rakocinski et al. 2016; White et al. 2018; Carmichael et al. 2019). Intermediate conditions between the end-members are characterized by non-red limestones with slightly lower Fe/Rb ratios compared to the red facies, very small or completely missing U and Mo enrichment, elevated concentrations of Ni, Cu, V and As (redox mode C, cycles 2, 5, 6 and 7), and/or by just a non-red colour and a minor enrichment in V and Cu (redox mode B, cycles 1,4 and 8). A similar alternation of layers with red, green-grey and dark grey colours and variations of redox-sensitive elements was reported by Bábek et al. (2021) from Lower Devonian MRB successions in the Prague Basin. They interpreted these layers as representing zones developing in the sediment subsurface with increasing depth along a redox gradient from oxic (Fe oxide Zone), to suboxic (Fe enrichment Zone, U–Mo enrichment Zone) and suboxic-anoxic conditions (Cu-V-Mo enrichment Zone). The thickness of the redox zones can be influenced by many factors including bottom oxygenation, sediment accumulation rates, rates of organic flux from the water column, and microbial assemblages and their activity within the sediment (Bábek et al. 2021; Munnecke et al. 2023).

Pulsating anoxia during the Frasnian/Famennian boundary interval.

The end-Frasnian (FZ10-FZ13) redox cyclicity shows a trend towards more anoxic conditions that peaked in the UKW horizon, followed by a trend (*Pa. triangularis* to *Pa. rhomboidea*) towards more oxic conditions (Fig. 7). These trends are consistent with the global trends of marine bottom anoxia from 15 sites around the globe (White et al. 2018). Upper Devonian sedimentary successions from South Laurussia, South China and North Gondwana are characterized by several recurrent periods of bottom hypoxia/anoxia (events) displaying a distinct lithology (dark to black carbonates and shales) and biodiversity losses or radiations (L. Frasnes, U. Frasnes, Timan, Middlesex, Rhinestreet, Semichatovae, LKW, UKW, Nehden, Condroz, Enkeberg, Annulata, Dasberg and Hangenberg events and several shorter fluctuations) (House 2002; Racki 2005; Becker et al. 2012; Gibb et al. 2024). The LKW and UKW horizons, in particular, were associated with widespread anoxia as suggested by organic-rich marine facies and various biological and geochemical proxies (Joachimski and Buggisch 1993; Murphy et al. 2000; Bond and Wignall 2008; Rakocinski et al. 2016; White et al. 2018; Carmichael et al. 2019). From the base-of-Frasnian (382.3 Ma) to early Famennian (*Pa. rhomboidea* Zone, ~ 367 Ma), ten such events occurred peaking in the UKW interval of global anoxia, indicating an average recurrence period of about 1.5 Myr, which is consistent with the summed recurrence intervals of the red-to-non-red couplets in our sections, ranging from ~ 0.85 Myr to ~ 2.0 Myr (see above). These fluctuations were non-periodic, and they did not correspond to the Milankovitch band, so they were likely not caused by orbital forcing. The development of this anoxia-governed stratigraphy has been attributed to transgressive–regressive pulses associated with coastal onlaps, seawater temperature fluctuations (warming and cooling), spreading of the Oxygen Minimum Zone (OMZ) onto continental shelves and intra shelf basins (bottom-up anoxia model), and anoxic overflows of dense waters originating by eutrophication of photic zone water in intra-shelf basins (top-down anoxia model) (House 2002; Crasquin and Horne 2018; Gibb et al. 2024, and references therein). The coincidence between the dysoxia/anoxia fluctuations with the UKW and LKW horizons, and their non-periodic nature suggests that their primary causes were the same that triggered the F/F mass extinction. These may include volcanic activity or bioevolutionary changes linked to the spread of vascular land plants (Racki et al. 2018; Song et al. 2017; Algeo and Shen 2024).

Most F/F sections of present-day Europe, North Africa and North America exhibiting the hypoxia-anoxia fluctuations, were located along the gradually closing Rheic Ocean seaway, and encircled by a chain of epicontinental basins of South Laurussia and North Gondwana. The complex oceanic current patterns implied by this palaeogeographic position, and interactions between the epicontinental basins and the oceanic seaway likely contributed to the vertical fluctuations of the OMZ (Crasquin and Horne 2018; Gibb et al. 2024). The biostratigraphic position of the redox cycles 2, 3, 5 and 8 in the Coumiac and Col des Tribes sections suggests that they can be assigned to the LKW, UKW, Nehden and Condroz bioevents, respectively, although there were clearly more fluctuations between them. It is assumed here that the redox fluctuations manifested in changing colour and redox geochemistry in the Montagne Noire sensitively responded to quasi-periodic vertical fluctuations in OMZ. Consequently, the colour characteristics of marine red beds can be considered a sensitive indicator of redox-related palaeoceanographic changes.

Conclusions

The Frasnian – lower Famennian marine red beds (MRB) of the Montagne Noire, including the "Griotte" facies were deposited in a low-energy outer ramp setting, below storm-wave base and photic zone, with occasional storm beds or turbidites. Their sedimentation rates were low, from ~ 1.7 to ~ 12.7 mm/kyr, which is typical for MRBs formed elsewhere.

The MRBs were hematitized (reddened) during very early diagenesis near the sediment–water interface, with a strong contribution from the activity of microaerophilic, Fe-oxidizing bacteria associated with microstromatolites, oncoidal structures, microborings and microproblematica (*Frutexites*). Hematite precipitation was closely coupled with authigenesis and alteration (biotic or abiotic) of Fe-bearing aluminosilicates produced through organomineralization. Submicron-sized hematite also occurs in the microsparite and in aluminosilicate-rich areas, likely formed by abiotic processes during early diagenesis.

The MRBs are enriched in hematite, but not necessarily in total Fe. Most Fe for the hematite growth was sourced from primary aluminosilicate minerals; its release from the source was also likely mediated by microbial activity. The hematitization occurred under oxic/microaerophilic bottom conditions, but the Fe release required development of reducing conditions along redox micro-gradients, which is indicated by the fluctuations in redox-sensitive elements, Fe, V, Cu, Mo and U in the red microstromatolites and microborings. The combination of a low-energy depositional environment, scarcity of benthic dwellers and slow sedimentation rates likely promoted the persistence of the redox (micro-)gradients contributing to the microbially mediated reddening.

The oxic seafloor conditions of MRBs during the Frasnian (FZ6) to early Famennian (*Pa. marginifera*) interval were punctuated by eight, ~ 0.5 to ~ 1.5 m thick layers representing intervals of dysoxia-anoxia, indicated by lack of hematite (non-red colour), precipitation of goethite instead, and enrichment in redox-sensitive As, V, Mo, Cu, Ni and U. Their recurrence interval ranged from ~ 0.85 Myr to ~ 2.0 Myr consistently with the Late Devonian bioevents reported from elsewhere, but this fluctuation was non-periodic. The Lower and Upper Kellwasser horizons are the most important examples, but an additional two are tentatively assigned to the early Famennian Nehden and Condroz events. Considering that they are seldom associated with lithological change, it is hypothesized that the bottom redox fluctuations developed owing to vertical fluctuations in Oxygen Minimum Zone that invaded the depositional environments.

Quantitative colour characteristics of marine red beds can be considered sensitive indicators of subtle, redox-related palaeoceanographic changes.

Supplementary Information The online version contains supplementary material available at https://doi.org/10.1007/s10347-025-00719-z.

Acknowledgements This research was funded from the Czech Science Foundation (GAČR) project 19-17435S. The study contributes to the Strategic Research Plan of the Czech Geological Survey (DKRVO/CGS 2023-2027, 311 650. We gratefully acknowledge Axel Munnecke for valuable discussions on microspar. We are grateful to Thomas J. Algeo and one anonymous reviewer for their helpful comments, and especially to Editor-in-Chief, Maurice E. Tucker for his careful editorial work, which helped us to significantly improve the quality of the manuscript.

Funding Open access publishing supported by the institutions participating in the CzechELib Transformative Agreement. Grantová Agentura České Republiky,19-17435S,Ondřej Bábek

Data availability All data that support the findings of this study are available in Supplementary Files. Samples and additional information are available upon request to the corresponding author [OB].

References

Aerden DGAM (1998) Tectonic evolution of the Montagne Noire and a possible orogenic model for syncollisional exhumation of deep rocks, Variscan belt, France. Tectonics 17:62–79

Algeo TJ, Li C (2020) Redox classification and calibration of redox thresholds in sedimentary systems. Geochim Cosmochim Acta 287:8–26

Algeo TJ, Shen J (2024) Theory and classification of mass extinction causation. Natl Sci Rev 11:nwad237

Algeo TJ, Tribovillard N (2009) Environmental analysis of paleoceanographic systems based on molybdenum–uranium covariation. Chem Geol 268:211–225

Algeo TJ, Berner RA, Maynard JB, Scheckler SE (1995) Late Devonian oceanic anoxic events and biotic crises: “rooted” in the evolution of vascular land plants. GSA Today 5:45–64

Algeo TJ, Remírez MN, Zhao H, Schwark L, Gordon G, Anbar A, Bates S, Lyons T, Over DJ, Sageman B (2025) Transient glacioeustatic fall and its climato-environmental effects during the Frasnian-Famennian transition. Glob Planet Change 256:105135

Arthaud F (1970) Etude tectonique et microtectonique compare´ e de deux domaines hercyniens: les nappes de la Montagne Noire (France) et l’anticlinorium de l’Iglesiente (Sardaigne). PhD thesis, Universite´ de Montpellier

Bábek O, Kalvoda J, Cossey P, Šimíček D, Devuyst F-X, Hargreaves S (2013) Facies and petrophysical signature of the Tournaisian/Viséan (Lower Carboniferous) sea-level cycle in carbonate ramp to basinal settings of the Wales-Brabant massif, British Isles. Sedim Geol 284–285:197–213

Bábek O, Faměra M, Hladil J, Kapusta J, Weinerová H, Šimíček D, Slavík L, Ďurišová J (2018) Origin of red pelagic carbonates as an interplay of global climate and local basin factors: insight from the Lower Devonian of the Prague Basin, Czech Republic. Sedim Geol 364:71–88

Bábek O, Vodrážková S, Kumpan T, Kalvoda J, Holá M, Ackerman L (2021) Geochemical record of the subsurface redox gradient in marine red beds: a case study from the Devonian Prague Basin, Czechia. Sedimentology 68:3523–3548

Bábek O, Kumpan T, Li W, Holá M, Šimíček D, Kapusta J (2022) Incipient reddening of Ordovician carbonates: the origin and geochemistry of yellow and pink colouration in limestones. Sedim Geol 440:106262

Becker TR, House MR (1994) Kellwasser events and goniatite successions in the Devonian of the Montagne Noire with comments on possible causations. Cour Forsch-Inst Senckenberg 169:45–77

Becker RT, Feist R, Flajs G, House MR, Klapper G (1989) Frasnian-Famennian extinction events in the Devonian at Coumiac, southern France. Compt Rend Acad Sci Paris 309:259–266

Becker RT, Gradstein FM, Hammer O (2012) The Devonian Period. In: Gradstein FM, Ogg JG, Schmitz MD, Ogg GM (eds) The Geologic Times Scale 2012, vol 2. Elsevier, Oxford, Amsterdam, Waltham, pp 559–601

Blakey RC, Ranney WD (2018). Ancient Landscapes of Western North America. https://doi.org/10.1007/978-3-319-59636-5_5

Bond DP, Wignall PB (2008) The role of sea-level change and marine anoxia in the Frasnian-Famennian (Late Devonian) mass extinction. Palaeogeogr Palaeoclimatol Palaeoecol 263(3):107–118

Buggisch W (1991) The global Frasnian-Famennian “Kellwasser Event.” Geol Rundsch 80:49–72

Cai Y, Hu Y, Li X, Pan Y (2012) Origin of the red colour in a red limestone from the Vispi Quarry section (central Italy): a high-resolution transmission electron microscopy analysis. Cretac Res 38:97–102

Carmichael SL, Waters JA, Königshof P, Suttner TJ, Kido E (2019) Paleogeography and paleoenvironments of the late Devonian Kellwasser event: a review of its sedimentological and geochemical expression. Glob Planet Change 183:102984

Chen D, Tucker ME (2003) The Frasnian-Famennian mass extinction: insights from high-resolution sequence stratigraphy and cyclostratigraphy in South China. Palaeogeogr Palaeoclimatol Palaeoecol 193:87–111. https://doi.org/10.1016/S0031-0182(02)00716-2

Chen D, Tucker ME, Shen Y, Yans J, Préat A (2002) Carbon isotope excursions and sea-level change: implications for the Frasnian-Famennian biotic crisis. J Geol Soc London 159:623–626. https://doi.org/10.1144/0016-764902-027

Cooper P (1986) Frasnian/Famennian mass extinction and cold-water oceans. Geology 14:835–839

Cooper RE, Wegner C-E, Kügler S, Poulin RX, Ueberschaar N, Wurlitzer JD, Stettin D, Wichard T, Pohnert G, Küsel K (2020) Iron is not everything: unexpected complex metabolic responses between iron-cycling microorganisms. ISME J 14:2675–2690. https://doi.org/10.1038/s41396-020-0718-z

Crasquin S, Horne DJ (2018) The palaeopsychrosphere in the Devonian. Lethaia 51:547–563

Da Silva A-C, Sinnesael M, Claeys P, Davies JHFL, de Winter NJ, Percival LME, Schaltegger U, De Vleeschouwer D (2020) Anchoring the late Devonian mass extinction in absolute time by integrating climatic controls and radio-isotopic dating. Sci Rep 10:12940

Day-Stirrat RJ, Aplin AC, Kurtev KD, Schleicher AM, Brown AP, Środoń J (2017) Late diagenesis of illite-smectite in the Podhale Basin, southern Poland: chemistry, morphology, and preferred orientation. Geosphere 13:2137–2153. https://doi.org/10.1130/GES01516.1

De Vleeschouwer D, Rakociński M, Racki G, Bond DPG, Sobień K, Claeys P (2013) The astronomical rhythm of Late-Devonian climate change (Kowala section, Holy Cross Mountains, Poland). Earth Planet Sci Lett 365:25–37

Deaton BC, Balsam WL (1991) Visible spectroscopy; a rapid method for determining hematite and goethite concentration in geological materials. J Sedim Petrol 61:628–632

Della Porta G, Webb GE, McDonald I (2015) REE patterns of microbial carbonate and cements from Sinemurian (Lower Jurassic) siliceous sponge mounds (Djebel Bou Dahar, High Atlas, Morocco). Chem Geol 400:65–86

Devleeschouwer X, Riquier L, Bábek O, De Vleeschouwer D, Petitclerc E, Sterckx S, Spassov S (2015) Magnetization carriers of grey to red deep-water limestones in the GSSP of the Givetian–Frasnian boundary (Puech de la Suque, France): Signals influenced by moderate diagenetic overprinting. In: Da Silva A-C, Whalen MT, Hladil J, Chadimova L, Chen D, Spassov S, Boulvain F, Devleeschouwer X (Eds) Magnetic Susceptibility Application: A Window Onto Ancient Environments and Climatic Variations, pp. 157–180. Geol Soc London Spec Publ 414, London

Devleeschouwer X (1999) La transition Frasnien-Famennien (Dévonien Supérieur) en Europe: sédimentologie, stratigraphie séquentielle et susceptibilité magnétique (Doctoral dissertation, Université de Lille I). 414

Ellwood BB, Crick RE, El Hassani A, Benoist SL, Young RH (2000) Magnetosusceptibility event and cyclostratigraphy method applied to marine rocks: detrital input versus carbonate productivity. Geology 28:1135–1138

Emerson D, Revsbech NP (1994) Investigation of an iron-oxidizing microbial mat community located near Aarhus,Denmark - field studies. Appl Environ Microbiol 60:4022–4031

Evans MA, Elmore RD (2006) Fluid control of localized mineral domains in limestone pressure solution structures. J Struct Geol 28:284–301

Feist R (1985) Devonian stratigraphy of the Southeastern Montagne Noire. Cour Forsch-Inst Senckenb 75:331–352

Feist R, Cornée JJ, Corradini C, Hartenfels S, Aretz M, Girard C (2021) The Devonian-Carboniferous boundary in the stratotype area (SE Montagne Noire, France). Palaeobio Palaeoenv 101:295–311. https://doi.org/10.1007/s12549-019-00402-6

Ferretti A, Cavalazzi B, Barbieri R, Westall F, Foucher F, Todesco R (2012) From black-and-white to colour in the Silurian. Palaeogeogr Palaeoclimatol Palaeoecol 367:178–192

Fortin D, Ferris FG, Scott SD (1998) Formation of Fe-silicates and Fe-oxides on bacterial surfaces in samples collected near hydrothermal vents on the Southern Explorer Ridge in the Northeast Pacific Ocean. Amer Mineral 83:1399–1408. https://doi.org/10.2138/am-1998-11-1229

Franke W, Paul J (1980) Pelagic redbeds in the Devonian of Germany—deposition and diagenesis. Sedim Geol 25:231–256

Franke W, Doublier MP, Klama K, Potel S, Wemmer K (2010a) Hot metamorphic core complex in a cold foreland. Int J Earth Sci (Geol Rundsch) 100:753–785

Franke W, Doublier MP, Klama K, Potel S, Wemmer K (2010b) Hot metamorphic core complex in a cold foreland. Int J Earth Sci 100:753–785

Gawlick HA, Suzuki H, Schlagintweit F (2006) The upper Triassic and Jurassic sedimentary rocks of the Sarsteinalm: evidence for the tectonic configuration of the Dachstein block (Salzkammergut region, Northern Calcareous Alps, Austria). N J Geol Palaeontol Abh 239:101–160

George AD, Chow N, Trinajstic KM (2014) Oxic facies and the Late Devonian mass extinction, Canning Basin, Australia. Geology 42:327–330. https://doi.org/10.1130/G35249.1

German CR, Elderfield H (1990) Application of the Ce anomaly as a paleoredox indicator: the ground rules. Paleoceanography 5:823–833. https://doi.org/10.1029/PA005i005p00823

Gibb MA, Hüneke H, Jadhav J, Gibb LM, Mehlhorn P, Mayer O, Aboussalam ZS, Becker RT, El Hassani A, Baidder L (2024) Contourite-drift archive links Late Devonian bioevents with periodic anoxic shelf water cascading. Geology 52:807–812. https://doi.org/10.1130/G52117.1

Giosan L, Flood RD, Aller RC (2002) Paleoceanographic significance of sediment color on western North Atlantic drifts: I. origin of color. Mar Geol 189:25–41

Girard C, Cornée J-J, Corradini C, Fravalo A, Feist R (2014) Palaeoenvironmental changes at Col des Tribes (Montagne Noire, France), a reference section for the Famennian of north Gondwana-related areas. Geol Mag 151:864–884. https://doi.org/10.1017/S0016756813000927

Gleason JD, Moore TC, Rea DK, Johnson TM, Owen RM, Blum JD, Hovan SA, Jones CE (2002) Ichthyolith strontium isotope stratigraphy of a Neogene red clay sequence: calibrating eolian dust accumulation rates in the central North Pacific. Earth Planet Sci Lett 202(3–4):625–636

Gorski CA, Aeschbacher M, Soltermann D, Voegelin A, Baeyens B, Marques Fernandes M, Hofstetter TB, Sander M (2012) Redox properties of structural Fe in clay minerals. 1. electrochemical quantification of electron-donating and accepting capacities of smectites. Environ Sci Technol 46:9360–9368. https://doi.org/10.1021/es3020138

Hanert HH (2002) Bacterial and chemical iron oxide deposition in a shallow bay on Palaea Kameni, Santorini, Greece: microscopy, electron probe microanalysis, and photometry of in situ experiments. Geomicrobiol J 19:317–342. https://doi.org/10.1080/01490450290098405

House MR (2002) Strength, timing, setting and cause of mid-Palaeozoic extinctions. Palaeogeogr Palaeoclimatol Palaeoecol 181:5–25

House MR, Kirchgasser WT, Price JD, Wade G (1985) Goniatites from Frasnian (Upper Devonian) and adjacent strata of the Montagne Noire. Hercynica 1(1):1–21

Hu X, Scott RW, Cai Y, Wang C, Melinte-Dobrinescu MC (2012) Cretaceous oceanic red beds (CORBs): different time scales and models of origin. Earth Sci Rev 115:217–248

Jansa L, Hu X (2009) An overview of the Cretaceous pelagic black shales and red beds: Origin, paleoclimate and paleoceanographic implications. In: (Hu X, Wang C, Scott RW, Wagreich M, Jansa L) Cretaceous Oceanic Red Beds: Stratigraphy, Composition, Origins and Paleoceanographic/Paleoclimatic Significance, SEPM Spec Publ 91, SEPM Soc Sedim Geol, Tulsa, OK. pp 59–72

Jenkyns HC, Hsü KJ (1975) Pelagic sediments: On land and under the sea an introduction. In: Hsu KJ, Jenkyns HC (eds) Pelagic Sediments: On Land and Under the Sea. IAS Spec Publ 1, Blackwell Publishing, Oxford pp 1–10

Jenkyns HC (1975) Origin of red nodular limestones (Ammonitico Rosso, Knollenkalke) in the Mediterranean Jurassic: A diagenetic model. In: Hsu KJ, Jenkyns HC (eds) Pelagic Sediments: On Land and Under the Sea. IAS Spec Publ 1, Blackwell Publishing, Oxford pp 249–271

Joachimski MM (1997) Comparison of organic and inorganic carbon isotope patterns across the Frasnian-Famennian boundary. Palaeogeogr Palaeoclimatol Palaeoecol 132:133–145

Joachimski MM, Buggisch W (1993) Anoxic events in the late Frasnian causes of the Frasnian Famennian faunal crisis? Geology 21:675–678. https://doi.org/10.1130/0091-7613(1993)021

Kalvoda J, Kumpan T, Holá M, Bábek O, Kanický V, Škoda R (2018) Fine-scale LA-ICP-MS study of redox oscillations and REEY cycling during the latest Devonian Hangenberg Crisis (Moravian Karst, Czech Republic). Palaeogeogr Palaeoclimatol Palaeoecol 493:30–43

Kang Y, Zhu R, Liu K, Zhang J, Zhang S (2024) Detrital and authigenic clay minerals in shales: a review on their identification and applications. Heliyon 10:e39239. https://doi.org/10.1016/j.heliyon.2024.e39239

Klapper G, Feist R, Becker R, House MR (1993) Definition of the Frasnian-Famennian stage boundary. Episodes 16(4):433–441

Klapper G (1989) The Montagne Noire Frasnian (Upper Devonian) conodont succession. In: McMillan NJ, Embry AF, Glass DJ (eds) Devonian of the World. Paleontology, Paleoecology, Biostratigraphy. Can. Soc. Petrol. Geol. Memoir 14 (III), Calgary 449–468

Konhauser KO, Fyfe WS, Ferris FG, Beveridge TJ (1993) Metal sorption and mineral precipitation by bacteria in two Amazonian river systems: Rio Solimões and Rio Negro, Brazil. Geology 21:1103–1106

Lasemi Z, Sandberg PA (1984) Transformation of aragonite-dominated lime muds to microcrystalline limestones. Geology 12(7):420–423

Le Houdec S, Girard C, Balter V (2013) Conodont Sr/Ca and δ18O record seawater changes at the Frasnian–Famennian boundary. Palaeogeogr Palaeoclimatol Palaeoecol 376:114–121

Lozano RP, Rossi C (2012) Exceptional preservation of Mn-oxidizing microbes in cave stromatolites (El Soplao, Spain). Sedim Geol 255:42–55. https://doi.org/10.1016/j.sedgeo.2012.02.003

Mamet B, Préat A (2006) Iron-bacterial mediation in Phanerozoic red limestones: state of the art. Sedim Geol 185:147–157. https://doi.org/10.1016/j.sedgeo.2005.12.009

Mamet B, Préat A, De Ridder C (1997) Bacterial origin of the red pigmentation in the Devonian Slivenec Limestone, Czech Republic. Facies 36:173–187

Marynowski L, Zatoń M, Rakociński M, Filipiak P, Kurkiewicz S, Pearce TJ (2012) Deciphering the upper Famennian Hangenberg black shale depositional environments based on multi-proxy record. Palaeogeogr Palaeoclimatol Palaeoecol 346–347:66–86

McLennan SM (2001) Relationships between the trace element composition of sedimentary rocks and upper continental crust. Geochem Geophys Geosyst 2:2000GC000109

Morford JL, Emerson SR (1999) The geochemistry of redox sensitive trace metals in sediments. Geochim Cosmochim Acta 63:1735–1750

Morford JL, Emerson SR, Breckel EJ, Kim SH (2005) Diagenesis of oxyanoins (V, U, R, and Mo) in pore waters and sediments from a continental margin. Geochim Cosmochim Acta 69:5021–5032

Munnecke A, Westphal H, Reijmer JJG, Samtleben C (1997) Microspar development during early marine burial diagenesis: a comparison of Pliocene carbonates from the Bahamas with Silurian limestones from Gotland (Sweden). Sedimentology 44:977–990. https://doi.org/10.1111/j.1365-3091.1997.tb02173.x

Munnecke A, Wright VP, Nohl T (2023) The origins and transformation of carbonate mud during early marine burial diagenesis and the fate of aragonite: a stratigraphic sedimentological perspective. Earth-Sci Rev 239:104366

Murphy AE, Sageman BB, Hollander DJ (2000) Eutrophication by decoupling of the marine biogeochemical cycles of C, N, and P: a mechanism for the Late Devonian mass extinction. Geology 28(5):427–430

Neuhuber S, Wagreich M, Wendler I, Spötl C (2007) Turonian oceanic red beds in the Eastern Alps: concepts for palaeoceanographic changes in the Mediterranean Tethys. Palaeogeogr Palaeoclimatol Palaeoecol 251:222–238

Orsi WD (2018) Ecology and evolution of seafloor and subseafloor microbial communities. Nat Rev Microbiol 16:671–683. https://doi.org/10.1038/s41579-018-0046-8

Préat A, Mamet B, Devleescholuwer X (1998) Sedimentology of the Frasnian-Famennian boundary stratotype (Coumiac, Montagne Noire, France). Bull Soc Geol Fr 3:331–342

Préat A, Mamet B, Bernard A, Gillan D (1999) Bacterial mediation, red matrices diagenesis, Devonian, Montagne Noire (southern France). Sedim Geol 126:223–242

Préat A, De Jong J, Mamet BL, Mattielli N (2008) Stable iron isotopes and microbial mediation in red pigmentation of the Rosso Ammonitico (Mid-Late Jurassic, Verona area, Italy). Astrobiology 8:841–857

Préat A, Mamet B, Di Stefano P, Martire L, Kolo K (2011) Microbially-induced Fe and Mn oxides in condensed pelagic sediments (Middle-Upper Jurassic, Western Sicily). Sed Geol 237:179–188. https://doi.org/10.1016/j.sedgeo.2011.03.001

Préat A, De Ridder C, Gillan D (2018) Bacterial origin of the red pigmentation of Phanerozoic carbonate rocks: an integrated study of geology-biology-chemistry. Geol Belg 21:167–175

Pujol F, Berner Z, Stüben D (2006) Palaeoenvironmental changes at the Frasnian/Famennian boundary in key European sections: chemostratigraphic constraints. Palaeogeogr Palaeoclimatol Palaeoecol 240:120–145

Qie W, Algeo TJ, Luo G, Herrmann A (2019) Global events of the Late Paleozoic (Early Devonian to Middle Permian): A review. Palaeogeography, Palaeoclimatology, Palaeoecology. 531, Part A, 109259

Racki G, Racka M, Matyja H, Devleeschouwer X (2002) The Frasnian/Famennian boundary interval in the South Polish−Moravian shelf basins: integrated event−stratigraphical approach. Palaeogeogr Palaeoclimatol Palaeoecol 181:251–297

Racki G, Rakociński M, Marynowski L, Wignall PB (2018) Mercury enrichments and the Frasnian-Famennian biotic crisis: a volcanic trigger proved? Geology 46:543–546. https://doi.org/10.1130/G40233.1

Racki G (2005) Toward understanding Late Devonian global events: few answers, many questions. In: Over DJ, Morrow JR, Wignall PB (Eds.) Understanding Late Devonian and Permian-Triassic Biotic and Climatic Events: Towards an Integrated Approach. Dev Palaeontol Stratigr 20:5–36

Rakociński M, Pisarzowska A, Janiszewska K, Szrek P (2016) Depositional conditions during the Lower Kellwasser Event (Late Frasnian) in the deep-shelf Łysogóry Basin of the Holy Cross Mountains Poland. Lethaia 49:571–590. https://doi.org/10.1111/let.12167

Rider MH (1999) The Geological Interpretation of Well Logs. Whittles Publishing Services, Dunbeath, p 288

Riquier L, Averbuch O, Devleeschouwer X, Tribovillard N (2007) Diagenetic versus detrital origin of the magnetic susceptibility variations in some carbonate Frasnian-Famennian boundary sections from Northern Africa and Western Europe: implications for paleoenvironmental reconstructions. Int J Earth Sci (Geol Rundsch) 99:57–73. https://doi.org/10.1007/s00531-009-0492-7

Rong J, Wang Y, Zhang X (2012) Tracking shallow marine red beds through geological time as exemplified by the lower Telychian (Silurian) in the Upper Yangtze Region, South China. Sci China Earth Sci 55:699–713

Rudnicki MD, Elderfield H (1993) A chemical model of the buoyant and neutrally buoyant plume above the TAG vent field, 26N, Mid-Atlantic Ridge. Geochim Cosmochim Acta 57:2939–2958

Schaefer MV, Gorski CA, Scherer MM (2011) Spectroscopic evidence for interfacial Fe(II)−Fe(III) electron transfer in a clay mineral. Environ Sci Technol 45:540–545. https://doi.org/10.1021/es102560m

Schindler E (1993) Event-stratigraphic markers within the Kellwasser crisis near the Frasnian/Famennian boundary (upper Devonian) in Germany. Palaeogeogr Palaeoclimatol Palaeoecol 104:115–125

Sepkoski JJ Jr (1982) Mass extinctions in the Phanerozoic oceans: a review. In: Silver LT, Schultz PH (Eds) Geological implications of impacts of large asteroids and comets on the Earth. Geol Soc Am Spec Paper 190:283–289

Smrzka D, Zwicker J, Bach W, Feng D, Himmler T, Chen D, Peckmann J (2019) The behavior of trace elements in seawater, sedimentary pore water, and their incorporation into carbonate minerals: a review. Facies 65:41

Song H, Song H, Algeo TJ, Tong J, Romaniello SJ, Zhu Y, Chu D, Gong Y, Anbar AD (2017) Uranium and carbon isotopes document global-ocean redox-productivity relationships linked to cooling during the Frasnian-Famennian mass extinction. Geology 45(10):887–890

Spalletta C, Perri MC, Over DJ, Corradini C (2017) Famennian (Upper Devonian) conodont zonation: revised global standard. Bull Geosci 92:31–57

Środoń J, Elsass F, McHardy WJ, Morgan DJ (1992) Chemistry of illite-smectite inferred from TEM measurements of fundamental particles. Clay Miner 27:137–158. https://doi.org/10.1180/claymin.1992.027.2.01

Steiner Z, Rae JWB, Berelson WM, Adkins JF, Hou Y, Dong S, Lampronti GI, Liu X, Achterberg EP, Subhas AV, Turchyn AV (2022) Authigenic formation of clay minerals in the abyssal North Pacific. Glob Biogeochem Cycles 36:e2021GB007270. https://doi.org/10.1029/2021GB007270

Straub KL, Benz M, Schink B, Widdel F (1996) Anaerobic, nitrate-dependent microbial oxidation of ferrous iron. Appl Environ Microbiol 62(4):1458–1460. https://doi.org/10.1128/aem.62.4.1458-1460.1996

Streel M, Caputo MV, Loboziak S, Melo JHG (2000) Late Frasnian-Famennian climates based on palynomorph analyses and the question of the Late Devonian glaciations. Earth-Sci Rev 52:121–173

Stumm W, Morgan JJ (1996) Aquatic Chemistry, 3rd edn. Wiley Interscience, New York, NY

Tremolada F, Bornemann A, Bralower TJ, Koeberl C, van de Schootbrugge B (2006) Paleoceanographic changes across the Jurassic/Cretaceous boundary: the calcareous phytoplankton response. Earth Planet Sci Lett 241:361–371

Tucker ME (1973) Ferromanganese nodules from the Devonian of the Montagne Noire (S. France) and West Germany. Geol Rundsch 62:137–153. https://doi.org/10.1007/BF01826821

Tucker ME (1975) Sedimentology of Palaeozoic Pelagic Limestones: The Devonian Griotte (Southern France) and Cephalopodenkalk (Germany). In: Hsü KJ, Jenkyns HC (eds) Pelagic Sediments: On Land and under the Sea. Wiley, pp 71–92. https://doi.org/10.1002/9781444304855.ch4

Van Groeningen N, Arrigo TLK, Byrne JM, Kappler A, Christl I, Kretzschmar R (2020) Interactions of ferrous iron with clay mineral surfaces during sorption and subsequent oxidation. Env Sci: Processes and Impacts 22:1355–1367. https://doi.org/10.1039/D0EM00063A

Van Groeningen N, Christl I, Kretzschmar R (2021) The effect of aeration on Mn(II) sorbed to clay minerals and its impact on Cd retention. Environ Sci Technol 55:1650–1658. https://doi.org/10.1021/acs.est.0c05875

Vodrážková S, Kumpan T, Vodrážka R, Frýda J, Čopjaková R, Koubová M, Munnecke A, Kalvoda J, Holá M (2022) Ferruginous coated grains of microbial origin from the Lower Devonian (Pragian) of the Prague Basin (Czech Republic) – petrological and geochemical perspective. Sedim Geol 438:106194. https://doi.org/10.1016/j.sedgeo.2022.106194

Vodrážková S, Koubová M, Munnecke A, Kumpan T, Vodrážka R, Pour O, Frýda J (2025) Clay mineral authigenesis as an example of organomineralization in Paleozoic coated grains and peloids. Sedim Geol 484:106912. https://doi.org/10.1016/j.sedgeo.2025.106912

Wagreich M, Krenmayr H-G (2005) Upper Cretaceous oceanic red beds (CORB) in the Northern Calcareous Alps (Nierental Formation, Austria): slope topography and clastic input as primary controlling factors. Cretac Res 26(1):57–64. https://doi.org/10.1016/j.cretres.2004.11.012

Wang K, Geldsetzer HHJ, Goodfellow WD, Krouse HR (1996) Carbon and sulfur isotope anomalies across the Frasnian-Famennian extinction boundary, Alberta, Canada. Geology 24:187–191

Wang C, Hu X, Sarti M, Sčoty RW, Li X (2005) Upper Cretaceous oceanic red beds in southern Tibet; a major change from anoxic to oxic, deep-sea environments. Cretac Res 26:21–32

Weiner T, Kalvoda J, Kumpan T, Schindler E, Šimíček D (2017) An integrated stratigraphy of the Frasnian-Famennian boundary interval (Late Devonian) in the Moravian Karst (Czech Republic) and Kellerwald (Germany). Bull Geosci 92:257–281

White DA, Elrick M, Romaniello S, Zhang F (2018) Global seawater redox trends during the late Devonian mass extinction detected using U isotopes of marine limestones. Earth Planet Sci Lett 503:68–77. https://doi.org/10.1016/j.epsl.2018.09.020

Widdel F, Schnell S, Heising S, Ehrenreich A, Assmus B, Schink B (1993) Ferrous iron oxidation by anoxygenic phototrophic bacteria. Nature 362:834–836

Wiederer U, Königshof P, Feist R, Franke W, Doublier MP (2002) Low-grade metamorphism in the Montagne Noire (S-France): conodont alteration index (CAI) in Palaeozoic carbonates and implications for the exhumation of a hot metamorphic core complex. Schweiz Mineral Petrogr Mitt 82:393–407

Zhang YG, Ji J, Balsam WL, Lianwen L, Chen J (2007) High resolution hematite and goethite records from ODP 1143, South China Sea: co-evolution of monsoonal precipitation and El Nino over the past 600,000 years. Earth Planet Sci Lett 264:136–150